

nlm.nih.gov/sites/sra) archives as E-MEXP-3798 and SRP017718, respectively. We thank A. Vodala, J. Menet, K. Abruzzi, and N. Francis for advice with techniques. Supported by a Wellcome Trust Senior Research Fellowship in Basic Biomedical Sciences, the Gatsby Charitable Foundation, Oxford Martin School and grants MH069883 and MH081982 from NIH (S.W.), NIH grants

NS044232 and NS045713 and the Ellison Medical Foundation (M.R.), and NIH grant R01HD049116 (Z.W. and W.T.).

#### Supplementary Materials

www.sciencemag.org/cgi/content/full/340/6128/91/DC1  
Materials and Methods

Figs. S1 to S6  
Tables S1 to S10  
References (45–49)

24 October 2012; accepted 1 February 2013  
10.1126/science.1231965

# Rats and Humans Can Optimally Accumulate Evidence for Decision-Making

Bingni W. Brunton,<sup>1,2\*</sup> Matthew M. Botvinick,<sup>1,3</sup> Carlos D. Brody<sup>1,2,4†</sup>

The gradual and noisy accumulation of evidence is a fundamental component of decision-making, with noise playing a key role as the source of variability and errors. However, the origins of this noise have never been determined. We developed decision-making tasks in which sensory evidence is delivered in randomly timed pulses, and analyzed the resulting data with models that use the richly detailed information of each trial's pulse timing to distinguish between different decision-making mechanisms. This analysis allowed measurement of the magnitude of noise in the accumulator's memory, separately from noise associated with incoming sensory evidence. In our tasks, the accumulator's memory was noiseless, for both rats and humans. In contrast, the addition of new sensory evidence was the primary source of variability. We suggest our task and modeling approach as a powerful method for revealing internal properties of decision-making processes.

Decisions in real life often need to be made based on noisy or unreliable evidence. Accumulating evidence from a set of noisy observations made over time makes it possible to average over different noise samples, thus improving estimates of the underlying signal. This principle is the basis for the influential class

of "drift-diffusion" models (1–5), which have been broadly applied to explain a variety of phenomena in biology (6–8). Accumulation involves both maintaining a memory of evidence accrued so far and adding new evidence to the memory. Yet no test to date has distinguished between noise associated with each of these two components.

We developed tasks in which subjects (humans and rats) were concurrently presented with two trains of pulses, one train representing "left"-labeled pulses and the other, "right"-labeled pulses. At the end of each trial, the subjects had to report which of the two trains had the greater total number of pulses. The timing of pulses was random and varied widely, both within and across individual trials (9, 10). We reasoned that the precisely known pulse timing would enable detailed modeling of the subjects' choices on each individual trial, whereas its variability would allow exploration of the stimulus space and would thus provide statistical power.

In an auditory version of the task, performed by three humans and 19 rats, left pulse trains were clicks presented on a speaker to the left of the subject, and right pulse trains were clicks presented on a speaker to the right of the sub-

<sup>1</sup>Princeton Neuroscience Institute, Princeton University, Princeton, NJ 08544, USA. <sup>2</sup>Department of Molecular Biology, Princeton University, Princeton, NJ 08544, USA. <sup>3</sup>Department of Psychology, Princeton University, Princeton, NJ 08544, USA. <sup>4</sup>Howard Hughes Medical Institute.

\*Present address: Department of Biology and Department of Applied Mathematics, University of Washington, Seattle, WA 98195, USA.

†Corresponding author. E-mail: brody@princeton.edu

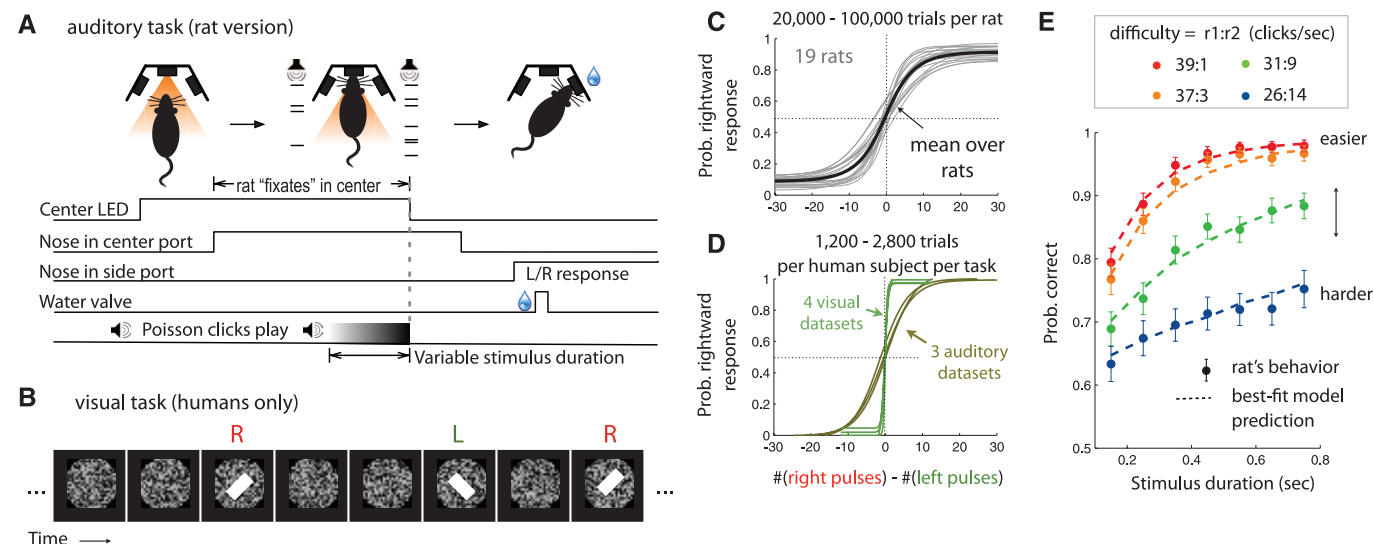


**Fig. 1. Psychophysical tasks and summary of behavior.** (A) Sequence of events in each trial of the rat auditory task. After light onset from a light-emitting diode (LED) in a center port, trained rats placed their nose into the port and "fixated" their nose there for a fixed amount of time until the light was turned off (1 to 2 s). Trains of randomly timed clicks were played concurrently from left and right free-field speakers during the last portion of the fixation time. After nose fixation and sounds ended, the rat made a choice, poking in the left or the right port to indicate which side played more clicks. Humans performed an analogous version of the task on a computer while

wearing headphones. (B) Schematic diagram of a stimulus in the visual pulses version of the task, performed by humans on a computer. (C) Psychometric curves (fits to a four-parameter logistic function for each subject; see methods) for rat subjects. (D) Psychometric curves, as in (C), for human subjects. (E) Chronometric curves for an example rat. Difficulty is labeled by the ratio of click rates played on the two sides. For each difficulty, performance improves with longer stimulus durations. Dashed lines show the best-fit model predictions for this rat, as described in the text. The vertical axis shows mean accuracy and 95% confidence interval (CI).

ject (Fig. 1A; free-field speakers for rats, headphones for humans). In a visual version of the task, performed by four humans, left pulses were flashed white bars, tilted anticlockwise from the vertical, and right pulses were flashed white bars tilted clockwise (3) (Fig. 1B). On each trial, the stimulus was presented for a duration controlled by the experimenter. The sum of the two pulse rates was kept fixed within each task, and discrimination difficulty was controlled on each trial by the ratio of the two rates (Fig. 1, C to E).

To examine a large variety of possible mechanisms consistent with the performance improvement at longer stimulus durations seen in Fig. 1E [(11, 12); see also fig. S4], we expanded on the drift-diffusion framework and implemented a flexible model (Box 1) in which different regimes of model parameter values represent widely different mechanisms (three examples in Fig. 2A), with mixtures of mechanisms represented by intermediate parameter values.

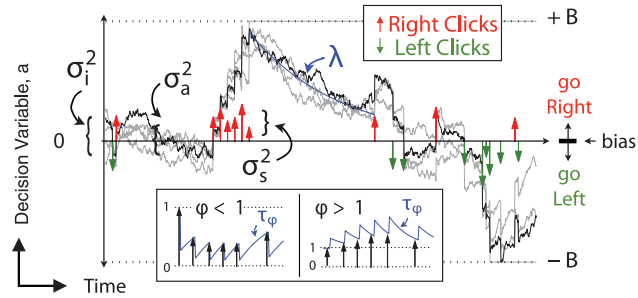
Given a trial's specific pulse times and a set of parameter values, the model produces the probability of observing a left versus a right response on that trial. Methods to compute the gradient of this probability with respect to model parameters (see the supplementary materials) were critical for efficiently finding the parameter values that gave the maximum likelihood of observing the complete set of a subject's responses. Numerical tests always found only one maximum (fig. S6), suggesting that we always found the global maximum. Consistent with this observation, a mathematically related model has been proven to have a concave log likelihood (6), suggesting that our model may also be provably concave and have a single maximum.

Figure 2, B to D, shows the likelihood landscape around best-fit (i.e., maximum-likelihood) parameters, given the data of a representative rat subject. Confidence intervals are given by the parameter width of the maximum (blue contours). Figure 2B shows  $\lambda$  ( $= 1/\tau$ , the memory time constant), which represents accumulator memory leak (if  $\lambda < 0$ ) or instability (if  $\lambda > 0$ ), and  $B$ , the height of the decision-commitment evidence bounds.  $\lambda$  was statistically indistinguishable from zero. That is, the decision dynamics were neither leaky nor unstable, suggesting that sensory evidence from throughout the entire stimulus period was given equal weight. The best-fit  $B$  was large enough that it produced model fits indistinguishable from those produced by  $B = \infty$ . Across subjects (Fig. 2, E and H), species, sensory modalities, and task parameters, the accumulator's memory time constant  $|\tau| = 1/|\lambda|$  was long ( $|\lambda| = 0.91 \pm 0.15 \text{ s}^{-1}$  mean  $\pm$  SE across rats;  $|\lambda| = 0.23 \pm 0.071 \text{ s}^{-1}$  across humans), in the sense that  $|\tau|$  was comparable to or greater than the longest stimulus duration used [1 s for rats, 4 s for humans (13)]. The best-fit values of  $B$  and  $\lambda$  were thus in the gradual accumulation regime (Fig. 2A, top).

In our tasks, noise in the sensory evidence ( $\sigma_s^2$ ) adds total variance proportional to the sum

of the amplitude of the clicks, whereas the memory diffusion noise ( $\sigma_a^2$ ) adds total variance proportional to the stimulus duration. This separability allows us to isolate the magnitude of the diffusion noise  $\sigma_a^2$  that gives the drift-diffusion model its name (2, 5). To our surprise, in 13 out of 19 rats and in all three humans performing the auditory task and all four humans performing the visual task, the value that best fit the data was the ideal  $\sigma_a^2 = 0$  (Fig. 2C for an example subject, Fig. 2, F and I, for all subjects). Consistent with the easily

distinguishable right versus left pulses used with humans, the best-fitting values of sensory evidence noise  $\sigma_s^2$  for humans were substantially lower than those for the rats (Fig. 2I). Again in this much lower  $\sigma_s^2$  regime, the best-fitting memory diffusion noise  $\sigma_a^2$  was zero. The dominant source of variability was thus noise in the evidence associated with each incoming pulse ( $\sigma_s^2 = 1.90 \pm 0.28 \text{ pulses}^2$  per incoming pulse for rats,  $0.50 \pm 0.059 \text{ pulses}^2$  in the human auditory task, and  $0.24 \pm 0.10 \text{ pulses}^2$  in the human visual task.)



#### Box 1.

At each time point, the accumulator memory  $a$  (black trace) represents an estimate of the right versus left evidence accrued so far. At stimulus end, the model decides right if  $a > \text{bias}$  and left otherwise, where bias is a free parameter. The light gray traces indicate alternate runs with different instantiations of model noise.

Right  $\uparrow$  (left  $\downarrow$ ) pulses change the value of  $a$  by positive (negative) impulses of magnitude  $C$ .

$\sigma_i^2$  parameterizes noise in the the initial value of  $a$ .

$\sigma_a^2$  is a diffusion constant, parameterizing noise in  $a$ .

$\sigma_s^2$  parameterizes noise when adding the evidence from a right or left pulse: For each click, variance  $\sigma_s^2$  is scaled by the amplitude of  $C$  and then added to the evidence contributed by the click.

$\lambda$  parameterizes consistent drift in the memory  $a$ . In the "leaky" or forgetful case ( $\lambda < 0$ , illustrated), drift is toward  $a = 0$ , and later pulses affect the decision more than earlier pulses. In the "unstable" or impulsive case ( $\lambda > 0$ ), drift is away from  $a = 0$ , and earlier pulses affect the decision more than later pulses. The memory's time constant  $\tau = 1/\lambda$ .

$B$  is the height of the sticky decision bounds and parameterizes the amount of evidence necessary to commit to a decision.

$\phi$  and  $\tau_\phi$  parameterize sensory adaptation by defining the dynamics of  $C$ . Immediately after a click, the magnitude  $C$  is multiplied by  $\phi$ .  $C$  then recovers toward an unadapted value of 1 with time constant  $\tau_\phi$ . Facilitation is thus represented by  $\phi > 1$ , whereas depression is represented by  $\phi < 1$  (inset).

These properties are implemented by the following equations

if  $|a| \geq B$  then  $da/dt = 0$ ; else

$$da = \sigma_a dW + (\delta_{t,t_R} \cdot \eta_R \cdot C - \delta_{t,t_L} \cdot \eta_L \cdot C) dt + \lambda a dt \quad (1)$$

where  $\delta_{t,t_{R,L}}$  are delta functions at the times of the pulses;  $\eta$  are i.i.d. Gaussian variables drawn from  $N(1, \sigma_\eta^2)$ ; and  $dW$  is a white-noise Wiener process. The initial condition  $a(t=0)$  is drawn from the Gaussian  $N(0, \sigma_i^2)$ .

Adaptation dynamics are given by

$$\frac{dC}{dt} = \frac{1-C}{\tau_\phi} + (\phi - 1)C(\delta_{t,t_R} + \delta_{t,t_L}) \quad (2)$$

In addition, a lapse rate parameterizes the fraction of trials on which a random response is made. Ideal performance ( $a = \text{\#right clicks} - \text{\#left clicks}$ ) would be achieved by

$$\lambda = 0, B = \infty, \sigma_i^2 = \sigma_a^2 = \sigma_s^2 = 0, \phi = 1, \text{bias} = 0 \quad (3)$$

This variability could be introduced by sensory uncertainty in the left-versus-right classification of each individual pulse, or by noise in the process of adding new sensory evidence to the accumulator memory.

The pulsatile nature of our task made it straightforward to parameterize sensory adaptation [(14); Eq. 2]. We found strong, quickly-recovering depression for rats (Fig. 2, D, G, and J; adaptation magnitude  $\phi = 0.17 \pm 0.021$ , recovery time constant  $\tau_\phi = 0.080 \pm 0.024$  s, mean  $\pm$  SE across rats). This is consistent with the depression observed in auditory cortex neural responses to click train stimuli (15, 16). Stimuli in the human tasks were constructed with a minimum inter-pulse interval (30 ms in the auditory task, 150 ms in the visual task), and this greatly reduced the adaptation effects as compared to those in rats (Fig. 2, G and J). Across all adaptation regimes, we found long accumulator time constants and zero memory diffusion noise.

If our subjects' behavior depends on a process that cannot be approximated by the model [such as collapsing bounds (17), variability in attention (18), or other possibilities not yet formalized in a model], our interpretation of the best-fit values may be problematic. We therefore tested the model-derived conclusions. To assess the memory time constant  $\tau$ , we calculated the "psychophysical reverse correlation" (17, 19–21), which estimates the extent to which click rates at each point in time influence left and right decisions. This analysis indicated that all periods of the trial have similar influence on the decision (approximately constant separation between the two traces in Fig. 3A), which is consistent with the long  $\tau$  found in the model-based analysis. To assess our estimates of the single-pulse noise  $\sigma_s^2$  and the starting variability  $\sigma_a^2$ , we fit the model to data from trials with multiple clicks on each of the two sides, and used those best-fit parameters to predict performance on trials in

which only one single-side pulse happened to be presented (for which performance is dominated by  $\sigma_s^2$  and  $\sigma_a^2$ ). The prediction was accurate, even on an individual subject-by-subject basis (Fig. 3B). To assess the memory diffusion noise  $\sigma_a^2$ , we controlled for sensory evidence by dividing trials into groups, so that all trials within a group had the same number of right clicks and the same number of left clicks; assuming large  $|\tau|$ , performance within each group is then dominated by  $\sigma_a^2$  and the click depression parameters  $\phi$  and  $\tau_\phi$ . Large  $\sigma_a^2$  would predict decreasing within-group performance at longer stimulus durations. The data showed the opposite trend and was precisely predicted by the best-fit model, where  $\sigma_a^2 = 0$  and clicks are depressing (Fig. 3C and fig. S13). The tests of Fig. 3 thus provided model-independent confirmation of the model-fit parameter values.

Using highly variable yet precisely known stimuli, together with a trial-by-trial model that

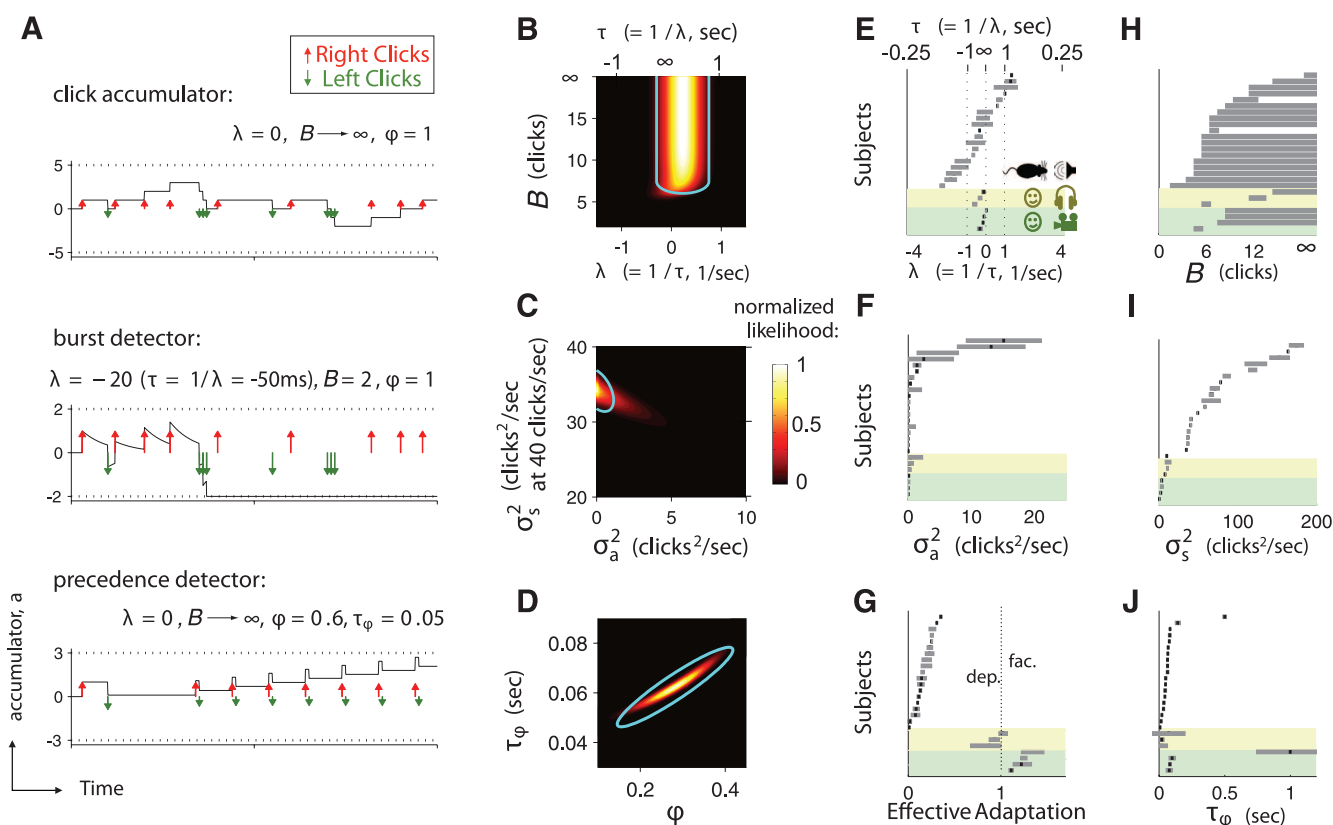


**Fig. 2. The model can fit a variety of mechanisms, but the data consistently fit to a pulse-accumulating mechanism with zero noise in the accumulator's memory.** (A) Three examples of the mechanisms that the model can represent. Top: The ideal, a pulse accumulator that weights all pulses equally. Middle: A burst detector. If three or more pulses from the same side arrive within 50 ms, the sticky bounds are reached, meaning that a commitment to orient to that side is made. Bottom: A precedence detector. If pulses from one side tend to arrive shortly before pulses from the other side, the adaptation minimizes the second side's pulses, and the decision tends toward the preceding side. (B to D) Parameter-likelihood landscapes that result from the data of one example rat. Panels are two-dimensional slices, cut through the full nine-dimensional parameter space, around the best-fit values. The blue curves represent CIs [2 SD of the multidimensional normal distribution fit to the

likelihood landscape (28)]. The best-fit parameter values found, which are  $\lambda \approx 0$ ,  $B \gg 1$ ,  $\sigma_a^2 \approx 0$ ,  $\sigma_s^2 \gg 0$ , and  $\phi \ll 1$ , correspond to pulse accumulation [(A), top] with a perfect memory but imperfect processing of sensory inputs. (E to J) Summaries of best-fit parameters over all subjects and tasks. Black ticks are best-fit values; gray bars span the CIs. Each panel has been divided by task (yellow highlight for human auditory task, green highlight for human visual task) and then sorted independently in order of parameter value. (E) All subjects, in all tasks, had long accumulator memories. (H) Most subjects were best fit with large bounds ( $B \rightarrow \infty$ ). (F) Thirteen of 19 rats and all humans in both auditory and visual tasks were best fit with  $\sigma_a^2 = 0$ . (I) A wide range of values, all large compared to  $\sigma_s^2$ , were found for  $\sigma_a^2$ . (G and J) All rats showed strong, rapidly recovering depression ( $\phi < 1$ , mean  $\tau_\phi = 0.040$  s). Humans showed weak depression in the auditory task and weak facilitation in the visual task.

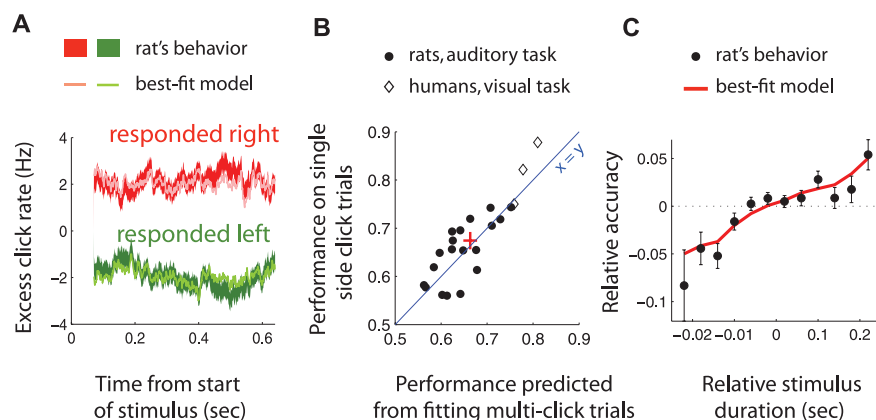


**Fig. 3. Model-independent analyses support model-fitting results.** (A) Long  $\tau$ : psychophysical reverse correlation for an example rat (longest quarter of trials only). For each time point in each trial, we computed the excess pulse rate difference (right pulses/s – left pulses/s, relative to the value expected given the random processes used to generate the trial) and then obtained an average for trials resulting in a right (red) and an average for trials resulting in a left (green) decision. The separation between the two indicates how strongly clicks from each time point influenced the final decision. Thick solid lines were obtained from the rat's responses; the thickness of the line represents the standard error. Narrow shaded lines were predicted by the best-fit model. (B) Accurate estimates of  $\sigma_s^2$  and  $\sigma_i^2$ : actual performance (fraction correct) on short-duration trials in which one side had one pulse and the other side had two pulses (i.e., trials for which performance was dominated by  $\sigma_s^2$  and  $\sigma_i^2$ ), versus performance predicted by fitting the model to trials with multiple pulses on each of the two sides. Too few trials of the short type to perform this analysis were presented for one of the human visual data sets and all human auditory data sets. Solid circles are individual rats, and open diamonds are individual humans. The red cross shows the mean and standard error across subjects. The accurate estimates of  $\sigma_s^2$  and  $\sigma_i^2$  suggested by the good predictions also suggest that  $\sigma_a^2$  was estimated accurately, because the sum  $\sigma_s^2 + \sigma_i^2 + \sigma_a^2$  is tightly constrained by the data (fig. S12). (C) Assessing  $\sigma_a^2$ ,  $\phi$ , and  $\tau_\phi$ : Trials were divided into groups, with sensory evidence and sensory noise controlled by keeping the total number of right clicks and the total number of left clicks fixed within each group. Performance within each group was then dominated by  $\sigma_a^2$ ,  $\phi$ , and  $\tau_\phi$ . (C) shows the performance of an example rat, averaged across trial groups and relative to the overall mean of each group, as a function of stimulus duration. The red line is the prediction from the best-fit model, with  $\sigma_a^2 = 0$ .

uses the full information about each trial's richly detailed stimulus (22), is a powerful approach for precisely quantifying multiple properties of decision-making processes. The approach provided strong evidence that rats can indeed gradually accumulate evidence for decision-making (23–26), thus establishing that this important cognitive phenomenon can be studied in a widely available animal model that is amenable to a rapidly growing arsenal of molecular tools.

With its capacity to provide moment-by-moment estimates of the temporal evolution of the accumulator, the approach will combine particularly well with neurobiological measurements. The model used for analysis can be readily expanded to consider and quantify further decision-making parameters, and the approach is easily generalized to different species, sensory modalities, and types of decision-making, including value-based decision-making (8, 27).

## References and Notes

1. R. Ratcliff, *Psychol. Rev.* **85**, 59 (1978).
2. S. W. Link, *The Wave Theory of Difference and Similarity* (Lawrence Erlbaum Associates, Mahwah, NJ, 1992).
3. M. Usher, J. L. McClelland, *Psychol. Rev.* **108**, 550 (2001).
4. R. Bogacz, E. Brown, J. Moehlis, P. Holmes, J. D. Cohen, *Psychol. Rev.* **113**, 700 (2006).
5. R. Ratcliff, G. McKoon, *Neural Comput.* **20**, 873 (2008).
6. L. Paninski, J. W. Pillow, E. P. Simoncelli, *Neural Comput.* **16**, 2533 (2004).
7. J. I. Gold, M. N. Shadlen, *Annu. Rev. Neurosci.* **30**, 535 (2007).
8. M. Milosavljevic, J. Malmaud, A. Huth, C. Koch, A. Rangel, *Judgm. Decis. Mak.* **5**, 437 (2010).
9. B. W. Brunton, C. D. Brody, paper presented at the Annual Meeting of the Society for Neuroscience, Chicago, IL, 18 October 2009.
10. J. I. Sanders, A. Kepecs, *J. Neurophysiol.* **108**, 3416 (2012).
11. A. B. Watson, *Vision Res.* **19**, 515 (1979).
12. J. Ditterich, *Neural Netw.* **19**, 981 (2006).
13. A. C. Huk, M. N. Shadlen, *J. Neurosci.* **25**, 10420 (2005).
14. B. Wark, B. N. Lundstrom, A. Fairhall, *Curr. Opin. Neurobiol.* **17**, 423 (2007).
15. D. Bendor, X. Wang, *Nat. Neurosci.* **10**, 763 (2007).
16. M. Wehr, A. M. Zador, *Neuron* **47**, 437 (2005).
17. R. Kiani, T. D. Hanks, M. N. Shadlen, *J. Neurosci.* **28**, 3017 (2008).
18. I. Krajbich, C. Armel, A. Rangel, *Nat. Neurosci.* **13**, 1292 (2010).
19. P. Neri, A. J. Parker, C. Blakemore, *Nature* **401**, 695 (1999).
20. H. Nienborg, B. G. Cumming, *Nature* **459**, 89 (2009).
21. D. Raposo, J. P. Sheppard, P. R. Schrater, A. K. Churchland, *J. Neurosci.* **32**, 3726 (2012).
22. J. W. Pillow et al., *Nature* **454**, 995 (2008).
23. N. Uchida, Z. F. Mainen, *Nat. Neurosci.* **6**, 1224 (2003).
24. N. M. Abraham et al., *Neuron* **44**, 865 (2004).
25. D. Rinberg, A. Koulakov, A. Gelperin, *Neuron* **51**, 351 (2006).
26. H. Zariwala, Z. F. Mainen, thesis, Stony Brook University, Stony Brook, NY (2007).
27. I. Krajbich, A. Rangel, *Proc. Natl. Acad. Sci. U.S.A.* **108**, 13852 (2011).
28. D. MacKay, *Information Theory, Inference, and Learning Algorithms* (Cambridge Univ. Press, Cambridge, 2003).

**Acknowledgments:** We thank Y. Niv for suggesting trial-by-trial analysis; D. Buonomano for suggesting we examine sensory adaptation; and A. Akrami, J. Erlich, C. Kopec, J. Kubanek, T. Hanks, B. Scott, M. Shadlen, D. Tank, and M. Yartsev for comments on the manuscript.

## Supplementary Materials

[www.sciencemag.org/cgi/content/full/340/6128/95/DC1](http://www.sciencemag.org/cgi/content/full/340/6128/95/DC1)

Methods

Supplementary Text

Modeling Methods

11 December 2012; accepted 1 February 2013

10.1126/science.1233912



Supplementary Materials for

**Rats and Humans Can Optimally Accumulate Evidence for Decision-Making**

Bingni W. Brunton, Matthew M. Botvinick, Carlos D. Brody\*

\*Corresponding author. E-mail: [brody@princeton.edu](mailto:brody@princeton.edu)

Published 5 April 2013, *Science* **340**, 95 (2013)  
DOI: 10.1126/science.1233912

**This PDF file includes:**

Methods  
Supplementary Text  
Modeling Methods  
References

# Rats and Humans can Optimally Accumulate Evidence for Decision-making

## *Supplementary Information & Methods*

Bingni W. Brunton, Matthew M. Botvinick & Carlos D. Brody

### Contents

<b>1</b>	<b>Behavior Methods</b>	<b>4</b>
1.1	Rat and human subjects . . . . .	4
1.2	The random pulses task: rat auditory, human auditory, and human visual versions . . . . .	4
1.2.1	Rats: Poisson clicks sound stimulus . . . . .	4
1.2.2	Humans: random clicks sound stimulus . . . . .	5
1.2.3	Humans: random flashes visual stimulus . . . . .	7
1.2.4	Rat behavioral box setup . . . . .	7
1.2.5	Rat behavioral training . . . . .	8
1.2.6	Human behavioral rig setup . . . . .	9
1.3	Psychometric and chronometric plots . . . . .	9
<b>2</b>	<b>Supplementary Information</b>	<b>11</b>
2.1	Related to main text Figure 1 . . . . .	11
2.1.1	Psychometric plots for each individual subject . . . . .	11
2.1.2	Chronometric plots for each individual subject . . . . .	11
2.1.3	Improvement as a function of stimulus duration for rat and for human task parameters	11



2.1.4	Burst detector, gradual accumulator, and other mechanisms can all produce similar chronometric curves . . . . .	11
2.2	Related to main text Box 1 . . . . .	14
2.3	Related to main text Figure 2 . . . . .	14
2.3.1	Table of best-fit parameters for each individual subject . . . . .	14
2.3.2	Plot of best-fit parameters and confidence intervals for each individual subject . .	17
2.3.3	Model has only one maximum likelihood point in parameter space . . . . .	19
2.3.4	Different subsets of data yield identical model fits . . . . .	20
2.3.5	Fitting model-generated data accurately recovers generating parameter values . . .	20
2.3.6	Model fits reliably recover small $\sigma_a^2$ , even in the presence of large $\sigma_s^2$ . . . . .	22
2.3.7	A restricted model where $\sigma_a^2 = 0$ and $B \rightarrow \infty$ is favored by AIC analysis . . . . .	22
2.3.8	Aspects of the data not well fit by the model . . . . .	22
2.4	Related to main text Figure 3 . . . . .	24
2.4.1	Result of model-free analyses for each individual subject . . . . .	24
2.4.2	Performance on single-click difference trials is well predicted by model fit to multi-click trials . . . . .	26
2.4.3	The data sharply constrains the model-fit total variance . . . . .	26
2.4.4	Testing $\sigma_a^2 = 0$ : Relative accuracy improved on trials with relatively longer stimulus durations. . . . .	27
<b>3</b>	<b>Modeling Methods</b>	<b>29</b>
3.1	Computing the probability of a response given a trial's model parameters and click times	29
3.1.1	The forward transition matrix for the discretized Fokker-Planck system . . . . .	32
3.1.1.1	Exact preservation of the evolution of the first moment of the distribution.	32
3.1.1.2	Determining $F_{ij}$ , the forward Markov transition matrix . . . . .	33
3.2	The gradient of the log likelihood of the model fit . . . . .	34
3.2.1	Gradient of the log likelihood of a model with hidden variables . . . . .	34

3.2.2	When the hidden variables are a Markov process . . . . .	35
3.2.3	Backward pass to compute the posterior distribution $P(a d, \theta)$ . . . . .	36
3.2.4	Rewriting into matrix notation for discretized spaces . . . . .	36
3.2.5	Differentiating the forward Markov transition matrix for an OU process . . . . .	38
3.2.6	Adding sticky decision bounds . . . . .	39
3.3	The gradient of the log likelihood of the model fit: Implementation . . . . .	40
3.3.1	The derivative with respect to accumulating and sensory noise . . . . .	40
3.3.2	The derivative with respect to noise in initial conditions . . . . .	41
3.3.3	The derivative with respect to sensory adaptation parameters . . . . .	41
3.3.4	The derivative with respect to bias and lapse rate . . . . .	42
3.4	Optimization of model parameters . . . . .	42
3.5	Confidence interval estimation of the best fit parameters . . . . .	43
3.5.1	An iterative projection method for computing ill-conditioned Hessians . . . . .	44
<b>4</b>	<b>Model-free analyses methods</b>	<b>45</b>
4.1	Psychophysical reverse correlation . . . . .	45
4.2	Burstiness analysis . . . . .	46
<b>5</b>	<b>Alternative Model: within-stream adaptation</b>	<b>48</b>



# 1 Behavior Methods

## 1.1 Rat and human subjects

Animal use procedures were approved by the Princeton University Institutional Animal Care and Use Committee and carried out in accordance with National Institute of Health standards. All animal subjects were male Long-Evans rats. Rats were pair-housed and kept on a reverse 12-hour light dark cycle; training occurred in the rats’ dark cycle, when they were more active. Rats were placed on a water restriction schedule to motivate them to work for water reward.

Human participants were four (4) Princeton undergraduates, three (3) of whom had normal hearing, all had normal or corrected-to-normal vision, and all gave their informed consent. Participants were paid to be part of the study and were naive to the main conclusions of the study. The consent procedure and the rest of the protocol were approved by the Princeton University Institutional Review Board.

## 1.2 The random pulses task: rat auditory, human auditory, and human visual versions

Task	typical trial presented	L + R pulse rate	Stimulus duration range	stimulus delivery	minimum IPI	$N_R - N_L$ variability
Rat auditory	$N_{\text{TOT}} = 22$ , $N_{\text{DIFF}} = 12$	40 pulses/sec	0.1 – 1.2 sec	free-field speakers	none	difference of Poissons
Human auditory	$N_{\text{TOT}} = 60$ , $N_{\text{DIFF}} = 7$ .	20 pulses/sec	2 – 4 sec	headphones	30 ms	sub-Poisson $\alpha = 0.8$
Human visual	$N_{\text{TOT}} = 14$ , $N_{\text{DIFF}} = 2$ .	4.5 pulses/sec (*)	2 – 4 sec	computer screen	150 ms	sub-Poisson $\alpha = 0.8$

Table 1: **The three tasks used.** In the “typical trial” column,  $N_{\text{TOT}}$  is the average number of right plus left pulses presented,  $N_{\text{DIFF}}$  is the average absolute difference between right and left. For each version of the task, performance on typical trials was  $\approx 80\%$  correct. (\*) subject R=3 pulses/sec in the visual task. See section 1.2.2 for explanation of sub-Poisson variability.

### 1.2.1 Rats: Poisson clicks sound stimulus

Randomly distributed click stimuli were played from both left and right speakers in the behavior training box, where each speaker played a series of clicks distributed as independent, Poisson events. Each “click” was a sum of pure tones (at 2, 4, 6, 8, and 16 kHz) convolved with a cosine envelope 3 msec in width. The sum of the expected click rates on left and right ( $r_L$  and  $r_R$ , respectively) was set at a constant

$r_L + r_R = 40$  (for rats) clicks per second. This range of rates was chosen to be low enough that the stimulus was perceived as clicks instead of a tone in humans [1] but high enough that counting clicks would be very difficult. (To our knowledge, this information is not available in rats.) The ratio  $\gamma = \log(r_R/r_L)$  was varied to generate Poisson click trains on each trial, where greater  $|\gamma|$  corresponded to easier trials, and smaller  $|\gamma|$  corresponded to harder trials.

In addition, in preliminary experiments, we observed that performance on trials of the shortest duration was better than performance on trials of intermediate duration (Fig. S1) and hypothesized that this phenomenon was due to the availability of an alternate, first click detection strategy. Subjects chose the side where the first click was played, which was highly correlated with the side with the higher click rate. To eliminate this confounding strategy for solving the perceptual task, the first click in each Poisson click train was always played in stereo, simultaneously on left and right sides.

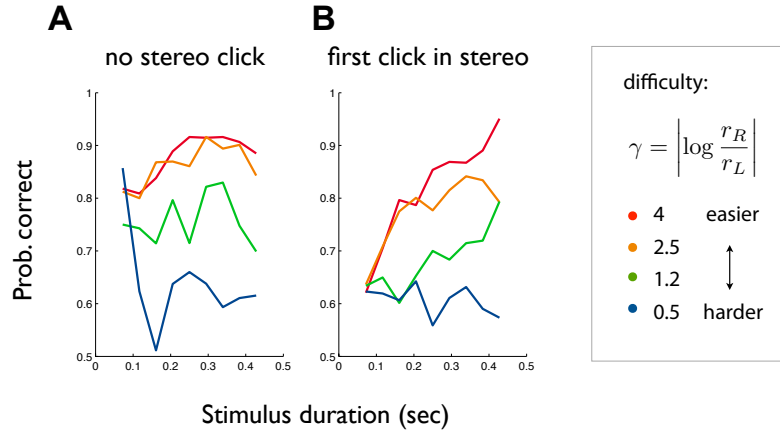


**Fig. S1: Preliminary data motivating the stereo click played at the beginning Poisson click trains.** In preliminary experiments, shown here for one example rat, performance on trials of the shortest duration was better than performance on trials of intermediate duration. This trend was eliminated when each Poisson click train started with a click played in stereo.

We determined the rewarded side for each trial based on the side where the greatest number of clicks was actually played, not on the underlying Poisson rates used to generate the clicks on that trial. In other words, because each Poisson click train was generated randomly, it is possible to have a trial where  $r_R > r_L$  but more clicks were played on the left than on the right ( $N_L > N_R$ ), in which case the left side was the rewarded response.

### 1.2.2 Humans: random clicks sound stimulus

Humans performed a task analogous to that of the rats on a computer, while wearing headphones. Clicks in the human auditory task were generated with a “refractory period” of 30 msec (*i.e.* a minimum inter-pulse interval (IPI) of 30 msec). This was done in the expectation that a 30 ms minimum IPI would minimize auditory adaptation effects (as indeed it did, main text Fig. 2g) and would thus probe whether other results depended on the presence of significant adaptation (they did not). For humans, the sum of the expected click rates on left and right was set at a constant  $r_L + r_R = 20$  clicks per second. This click

rate, lower than that of the rats, was chosen to have a typical inter-pulse interval (50 ms) substantially longer than the 30 msec minimum IPI. This was necessary to allow significant randomness in the pulse timing while adhering to the 30 ms minimum IPI constraint. The use of human subjects facilitated probing longer stimulus durations than with the rats: stimulus durations ranged from 2 to 4 sec.

*Sub-Poisson variability in click differences for humans*. When wearing headphones humans performed the task very well (as predicted from the model under the assumption that wearing headphones would lead to a small  $\sigma_s^2$ ). At a left:right pulse ratio of 1:1, namely 10 clicks/sec on each ear (20 clicks/sec total) over 4 seconds, humans had a psychophysical threshold of  $\approx 7$  clicks (main text, Fig. 1d; Fig. S2). However, stimuli generated by Poisson processes at these rates produce trials with a typical click difference  $|N_R - N_L|$  of  $\approx 9$  clicks (this is the standard deviation of the difference of two Poissons with means 40 each). Because most Poisson-generated trials therefore had a click difference greater than the subjects' threshold, most Poisson-generated trials were performed correctly. While this behavior was consistent with our prediction that use of headphones should reduce the single-pulse noise  $\sigma_s^2$  and therefore markedly increase performance, it left little behavioral variability for the model to use for distinguishing between different mechanisms. To circumvent this problem, we generated trials that had variability in the click difference  $N_R - N_L$  that was lower than what would be expected from the difference of two Poisson processes: on each trial, the total number of pulses to be played was generated from a Poisson distribution with rate  $T \cdot (r_L + r_R)$ , where  $T$  was the desired total stimulus duration. The difference  $N_R - N_L$  was then sampled from a Gaussian distribution that had a mean  $\mu = T \cdot (r_R - r_L)$  and variance  $\alpha \cdot T \cdot (r_R + r_L)$ . This last is equal to the variance of the difference of the two Poisson distributions, multiplied by a factor  $\alpha$ . We used  $\alpha = 0.8$ , i.e., 80% of the variability expected from Poisson-generated trials. Once  $N_R + N_L$  and  $N_R - N_L$  were sampled for a trial, this determined  $N_R$  and  $N_L$ . The timing of each click was then randomly assigned to the interval  $(0, T)$  (with the constraint that no two clicks could be within less than 30 ms of each other). In contrast to the Poisson-generated pulse trains used in the rat auditory task, accumulator models do not necessarily predict an increase in performance with stimulus duration for pulse trains generated with sub-Poisson variability in  $N_R - N_L$ .

*Instructions and "training" of human subjects*. Human subjects were told that the correct response depended on which side had the greater total number of pulses, regardless of when those pulses arrived during the trial. Subjects were not instructed as to what strategy to use for determining their response. Typical sessions had 200 trials each. Performance was observed to increase over sessions. As performance increased, the ratio of left and right pulse rates was decreased, so as to keep performance approximately at 80% correct. Data from sessions before performance plateaued was not used in the analysis. Approximately 4000 trials were collected per task per subject ( $\approx 20$  sessions/subject), of which the first 2000 trials were discarded from the analysis because performance had not yet plateaued.

Obtaining large numbers of trials is more difficult with humans than with rats. For this reason, we used only a single, low log ratio value  $\gamma = \left| \log \frac{r_R}{r_L} \right|$  for each human (see Fig. S3), set at a value that produced approximately 80% correct performance. We found that the data obtained with this single difficulty level (as set by  $\gamma$ ) sufficient to constrain the model, as indicated by reasonably small confidence intervals in the parameter estimates (Fig. S5). This amount of data still allowed clearly distinguishing between different sources of variability ( $\sigma_a^2$  vs.  $\sigma_s^2$ ).

### 1.2.3 Humans: random flashes visual stimulus

Humans participants also performed a visual version of the task, as illustrated in Fig. 1b. Flashed white bars tilted  $45^\circ$  anti-clockwise from vertical were considered evidence for a Left response, and flashed white bars tilted  $45^\circ$  clockwise from vertical were considered evidence for a Right response. To minimize the information that any single pixel would provide, and require detecting the orientation of the bars, the center of each white bar flash was offset randomly relative to the center of the circular white noise mask, where the offset (in horizontal and vertical directions) was drawn for each frame from a Gaussian distribution with a standard deviation equivalent to 3% of the diameter of the mask.

The visual stimulus was updated on a computer display at 30 cycles per second and consisted of a dynamic, circular white noise mask at the center of the display. Overlaid on this white noise mask, high-contrast tilted white bars were flashed at random times, each for a duration of one frame (0.033 sec). Flash events had a minimum inter-pulse interval of 0.15 sec (4-5 frames). This was chosen so as to be larger than the range where visual flicker fusion is known to occur. Given this minimum inter-pulse-interval, a total flash rate of  $r_L + r_R = 4.5$  events per second (subjects D, J, and K) or  $r_L + r_R = 3$  events per second (subject R), was used, which led to a typical interpulse interval longer than the minimum IPI of 0.15 sec, and thus allowed randomness in pulse timing. Long stimulus durations (2 to 4 sec) were used to minimize the possibility that subjects could keep track of the precise integer number of flashes presented. In post-hoc interviews, subjects did not report using an integer counting strategy, but instead reported using an overall accumulation strategy (e.g., “an overall sense of which side had more pulses”).

As with the human auditory task, sub-Poisson variability in  $N_R - N_L$  was used in the visual task, with a sub-Poisson factor  $\alpha = 0.8$ . Performance increased over sessions, and data from sessions before performance plateaued was discarded from the analysis.

As with the human auditory task, we used only a single, low log ratio value  $\gamma = \left| \log \frac{r_R}{r_L} \right|$  with humans (see Fig. S3), set at a value that produced approximately 80% correct performance. The data obtained with this single difficulty level (as set by  $\gamma$ ) was sufficient to constrain the model, as indicated by reasonably small confidence intervals in the parameter estimates (Fig. S5).

### 1.2.4 Rat behavioral box setup

Behavior took place in a custom training box inside a sound and light attenuated chamber. Each box had three “nose ports” arranged side-by-side along a curved wall. The center port had a cylindrical opening, so that rats could insert their entire snout into the opening; the side ports were conical. Pokes were detected with an infra-red (IR) beam across the front of each nose port. Each nose port also had a visible white light emitting diode (LED). The side nose ports each have a sipper tube, where water delivery was controlled by a solenoid. Two speakers were mounted above the left and right nose ports, respectively, allowing delivery of sounds in stereo. All behavioral, stimulus, and reward events were timestamped with greater than 1 msec accuracy using a custom open-source software (open-source code at <http://code.google.com/p/rt-fsm/>) on a computer running a realtime linux operating system. Rats

were placed into and removed from the training box by technicians who were blind to the task.

### 1.2.5 Rat behavioral training

Rats were trained using an automated training protocol. Approximately three quarters (3/4) of naive rats progress successfully through this pipeline and perform the full task after 4-6 months of daily training. Rats were trained in daily sessions of approximately 90 minutes and perform 200-500 trials per session.

In stage 1, naive rats were first shaped on a classical conditioning paradigm, where they associated water delivery from the left or right nose port with localized, regular click trains played out of the left or right speakers, respectively. After rats reliably poked in the side port, they were switched to a basic instrumental paradigm; a localized sound predicted the location of the reward, and rats had to poke in the appropriate side port within a shortening window of time in order to receive the water. Trials had inter-trial intervals of 1-2 minutes. For the first 4 days, water was delivered only on one side per session (*i.e.*, day 1: all Left; day 2: all Right; etc.). On subsequent days, Left and Right trials were interleaved randomly. This initial stage in the training lasted for a minimum of one week, but was as long as 3 weeks.

In stage 2, the rats were trained to initiate trials by poking in the center nose port. A light in the center port indicated that the rat should poke there, which triggered the presentation of a localized click train. The clicks were Poisson distributed, but played only out of one speaker, so that the discrimination was very easy. Incorrect responses were punished with a short time-out. Rats learned that the location of the sound predicted the location of the reward. In each session, trials were first presented in blocks of left and right trials, moving onto randomly interleaved left and right trials after a set number of blocked trials had been completed. As a rat showed basic proficiency in this task structure, usually after 4-7 days, it was moved to fully interleaved trials for the entire session.

Stage 3 in the training was enforcing the center “fixation period.” At first, the rat needed to break the center port IR beam for 200 msec before withdrawing and making a side response. Over time, this minimum required time grew slowly, so that the rat was required to hold its nose in the center port for longer periods of time before allowed to withdraw. The minimum required fixation time grew by 0.5 msec at every successfully complete center poke fixation trial. As the center fixation requirement grew, the onset of the sound stimulus was delayed such that the sound always played during the last 400 msec of the fixation. The offset of the clicks coincided with the offset of the center light, both of which cued the rat that it was allowed to make its side response. Earlier in the task development, rats were trained to center fixate for 1 sec; rats are now routinely trained to center fixate for 2 sec. Premature exit from the center port was indicated with a loud sound, punished with a short (200 msec) time-out, and the rat was required to re-initiate the center fixation. Rats learned center fixation after 3-8 weeks, achieving violation (premature exit from center port) rates of 20-40%. Unless indicated otherwise, these violation trials were ignored in all subsequent behavioral and model-fitting analyses.

At the end of this stage, rats were center port fixating for 2 seconds with <40% fixation violations and performed simple auditory discrimination of 400 msec localized click trains at >80% accuracy. Approximately 1/4 rats who started training on the Poisson click task failed to reach this criterion and did not proceed to the next stage in the training.

The final stage (stage 4) in the training introduced the full range of more difficult discriminations (see section 1.2.1) played for various durations. The shortest sounds were 100 msec in duration, and the longest sounds were up to 1000 msec, where the range was fixed for each rat. The duration of the sound on each trial was drawn uniformly from this range, and as in the previous training stage, the delay from the beginning of fixation to the onset of the sound was determined such that the offset of the sound always coincided with the offset of the center light. The range of difficulties ( $\gamma$ 's, see section 1.2.1) was adjusted for each rat such that it experienced at least 3 different difficulties and its mean accuracy over a session was 70–85%.

### 1.2.6 Human behavioral rig setup

Human participants performed the task in a small, closed room. A computer running Matlab controlled stimulus delivery through custom-written software using Psychophysical Toolbox ([www.psychtoolbox.org](http://www.psychtoolbox.org)). Visual stimuli were shown on a LCD computer display with a frame rate of 60 Hz. For the visual task, they were instructed to place themselves in a head-chin rest, which was set to maintain 55 cm between the plane of the eyes and the plane of the computer monitor. All visual stimuli were shown at 30 Hz. Auditory stimuli were delivered via over-the-ear headphones (Auvio Model CH139-AAI01). Subjects interacted with the behavioral software using a standard keyboard.

Each human trial began when the subject pressed the ‘Space’ key to indicate readiness. A fixation cross was displayed to indicate the beginning of the fixation period, and a randomly generated stimulus was presented after a variable delay. The end of the stimulus was signaled with the offset of the fixation cross, at which time the subject is free to press the ‘s’ key to indicate a Left response or the ‘l’ key to indicate a Right response. Reaction times of longer than 1 seconds were considered time-outs and those trials were ignored. Premature responses (before the end of the stimulus presentation) were also ignored. After their response, subjects received feedback about whether they were correct or incorrect both on the screen and with an auditory cue (a ding-ling sound for correct responses and a buzzer for incorrect responses). On trials with no well-defined correct response (i.e., trials where there were the same number of Left and Right pulses), the feedback to the human participant was determined randomly. After a correct response, the subsequent trial was ready immediately; incorrect responses were followed by a short, two-second time-out.

Subjects received feedback about their mean accuracy over the session with a numerical display that appeared after every tenth trial. Subjects were instructed to perform at least 200 auditory trials or 150 visual trials per session, and their payment was determined by their mean accuracy over that session such that higher accuracy meant higher pay per correct answer over a certain base amount. At the end of each session, each subject received an automated summary of their performance and payment for that session. After a few initial training sessions, subjects maintained above 80% accuracy on most sessions, and only these sessions after stable performance was achieved were used for the analysis.

## 1.3 Psychometric and chronometric plots

Psychometric plots (as shown in Fig. 1c,d and Fig S2) show the probability of the subject responding rightward as a function of the difference in number of right clicks and number of left clicks  $N_R - N_L$ . The

fits were to a 4-parameter logistic function of the form

$$y(x) = y_0 + \frac{a}{1 + \exp\left(\frac{-(x-x_0)}{b}\right)} \quad (1)$$

where  $y_0$  is the left endpoint,  $y_0 + a$  is the right endpoint,  $x_0$  is the bias, and  $a/4b$  is the slope. Fits were non-linear least-square regressions done using the `nlinfit.m` function from Matlab.

Chronometric plots (as shown in Fig. 1e and Fig. S3) sort the behavioral responses on each trial based on the difficulty of the discrimination. Difficulty was defined as the ratio  $|\gamma| = |\log(r_R/r_L)|$ , as described in section 1.2.1, and approximates the mean evidence available per unit time. The stimulus duration was computed as the duration of the sound played during the trial *minus* the timing of the first click played, since it would be impossible for the subject to detect the start of the sound before the first click. Trials of each difficulty were further binned by duration in 100 msec bins. The vertical axis shows the mean accuracy; error bars are 95% confidence intervals, assuming a binomial distribution.

The identical procedure was used to produce model-predicted curves, where the model-predicted probability correct on each trial was used instead of the subjects' responses.



## 2 Supplementary Information

### 2.1 Related to main text Figure 1

#### 2.1.1 Psychometric plots for each individual subject

Psychometric plots for each individual subject, corresponding to Fig. 1c and 1d of the main text, are shown in Fig. S2. Details of methods used to obtain these plots are found in Section 1.3. Fig. S2 also notes the number of trials used in the analysis for each subject for each task.

#### 2.1.2 Chronometric plots for each individual subject

Chronometric plots for each individual subject, corresponding to Fig. 1e of the main text, are shown in Fig. S3. Details of methods used to obtain these plots are found in Section 1.3.

#### 2.1.3 Improvement as a function of stimulus duration for rat and for human task parameters

For pulse trains generated by Poisson processes, accumulator models with an infinite accumulation time constant  $\tau$  predict that performance should improve as a function of stimulus duration. For the rat auditory task, pulse trains were generated by Poisson processes, and the expected improvement as a function of stimulus duration is seen in the data (Fig. 1, and Fig. S3).

However, when the trial-to-trial variability in the net evidence is constrained to be small, as it was in the case of the human tasks (Methods 1.2.2), accumulator models do not necessarily predict increased performance at increased stimulus durations. An extreme case serves to illustrate this: if the difference in the number of clicks  $N_R - N_L$  is constrained to be one on every trial, then the noise will grow as a function of stimulus duration or number of pulses, but the signal is constrained to be constant at 1, and therefore the signal-to-noise ratio *decreases* at longer stimulus durations, and so will performance. Thus, in the human tasks we do not necessarily expect performance to increase with duration. We found that with the a sub-Poisson variability factor of  $\alpha = 0.8$ , human performance stayed approximately constant as a function of stimulus duration, and this was well-matched by the model (compare dashed lines to solid data points, human panels at lower right of Fig. S3).

#### 2.1.4 Burst detector, gradual accumulator, and other mechanisms can all produce similar chronometric curves

The name “chronometric plot” refers to a plot of performance versus stimulus duration (Fig. 1e of main text; [2]). Performance that improves as stimulus duration grows has been reported for a variety of subjects on a number of different tasks, and has been considered by many to be a signature of noisy accumulation as the mechanism underlying decision-making [2, 3]. However, alternate decision-making mechanisms have been proposed that motivate a more detailed examination of the decision dynamics. In the random dot

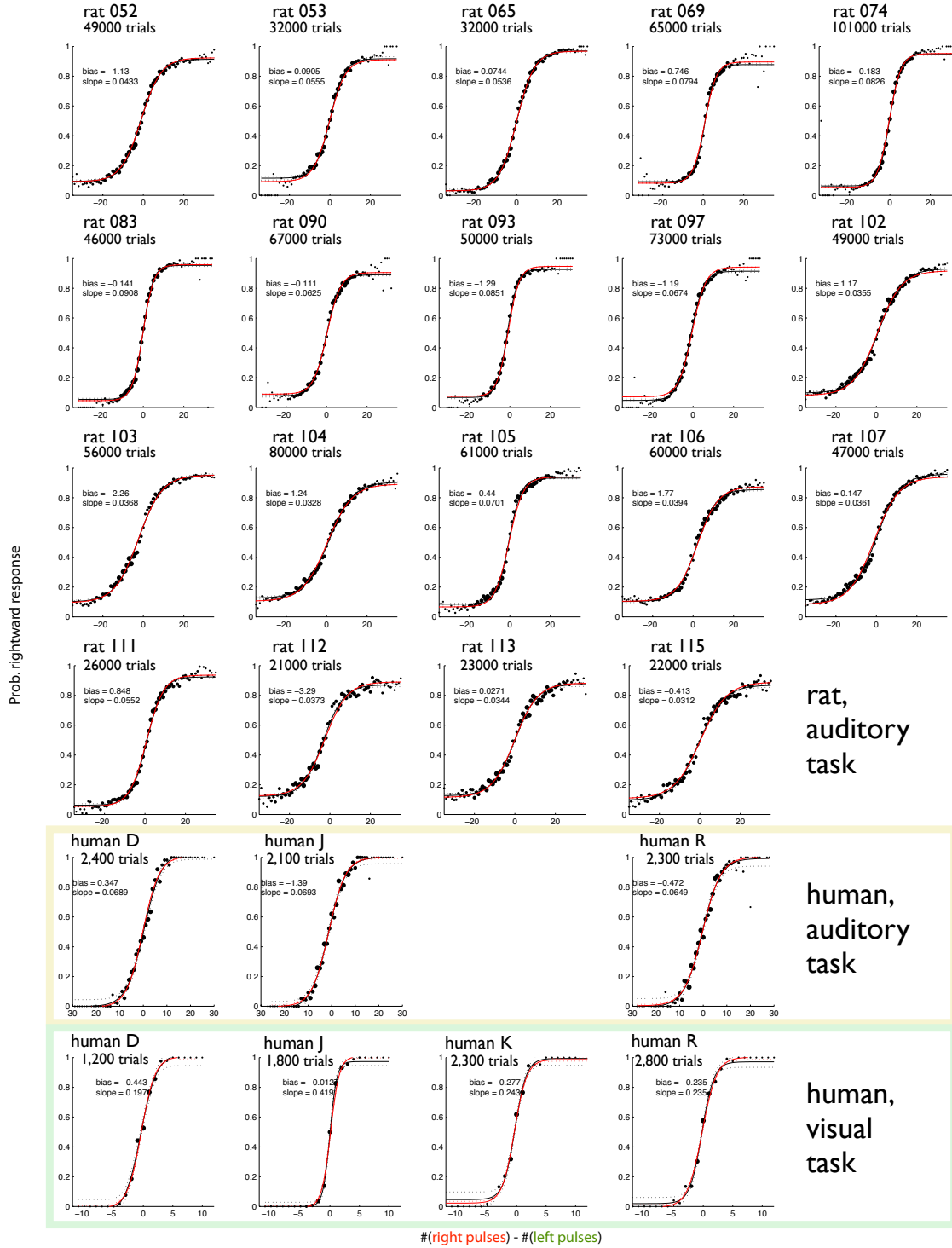


**Fig. S2: Psychometric plots for all subjects.** The size of each black dot is proportional to the number of trials included in that data point. The black line is a fit of the averaged raw data to a 4-parameter logistic function, where the bias and slope of the logistic fit is shown for each rat. The red line is the psychometric curve predicted by the best-fit model for each subject, as described in section 3.

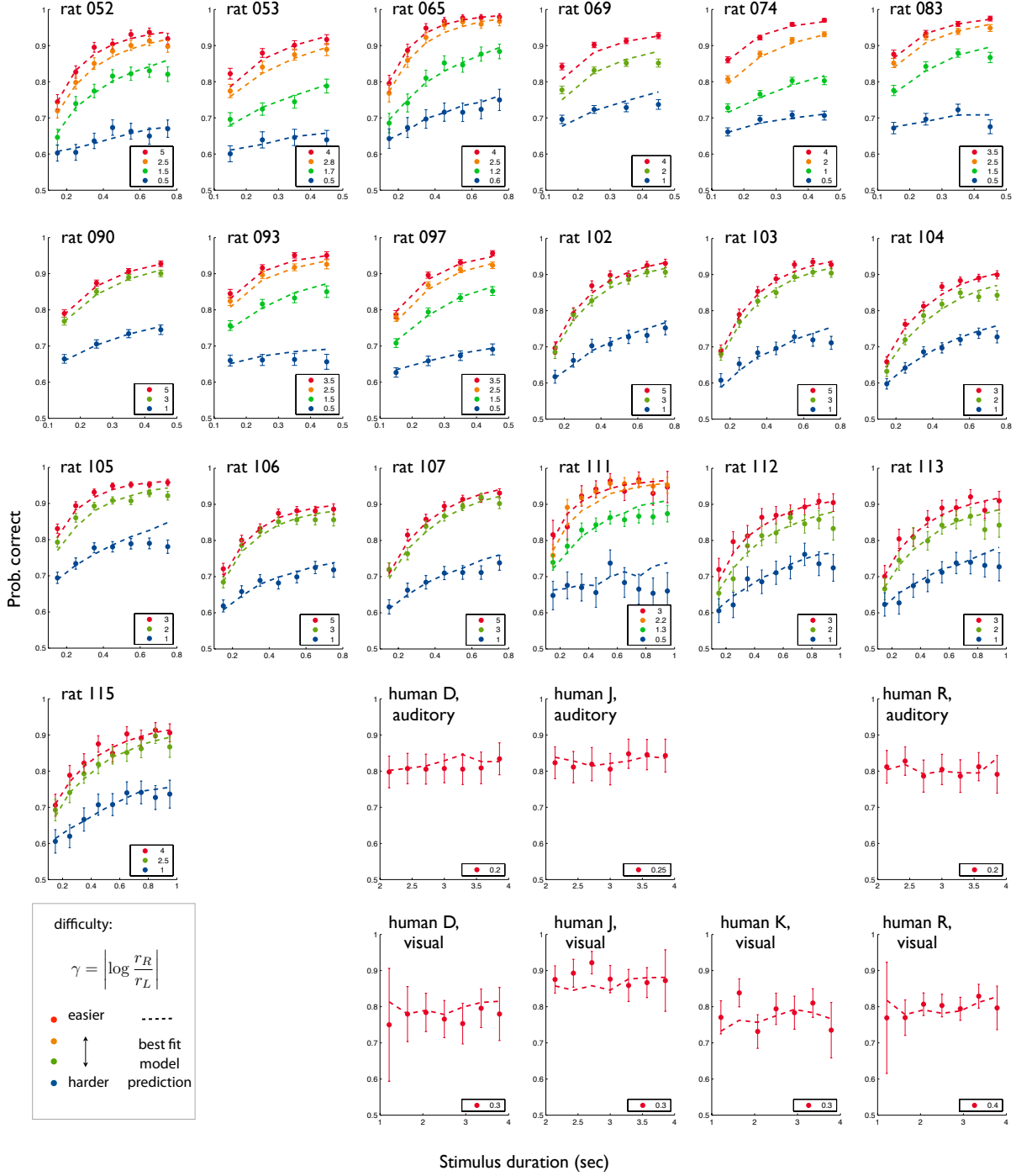


**Fig. S3: Chronometric plots and model fits for all subjects.** Each plots shows performance as a function of stimulus duration for each difficulty. The dashed lines show the best-fit model predictions for each rat, as described in section 3. The vertical axis shows mean accuracy  $\pm 0.95$  c.i. Accumulator models predict an increase in performance at greater stimulus durations for Poisson-generated pulse trains, as was the case for the rat auditory task. In contrast, accumulator models do not necessarily predict an increase in performance with stimulus duration for pulse trains generated with sub-Poisson variability in the click difference  $N_R - N_L$ , as was the case for pulse trains in the human tasks. (See Supp. Info. 2.1.4 and methods section 1.2.2.)

motion task [4], behavioral data well fit with drift-diffusion-type models [5] may also be consistent with a burst-detection mechanism [6]. Following this view, we find that for the task performed by the rats, noisy accumulation is not the only mechanism consistent with improved performance at longer stimulus durations. Using the model from Box 1 of the main text, Fig. S4 shows the chronometric plots produced when parameters are set to values that represent at a variety of different mechanisms. An accumulator of clicks and a burst detector (illustrated in Fig. 2a of main text) both lead to performance improvement at longer durations; as do various other mechanisms. As stated in the main text, improved performance at longer stimulus durations is not sufficient to conclude that subjects are using an evidence accumulation mechanism. In addition, the chronometric plot alone cannot differentiate between different sources of noise (Fig. S4e, f, g).

## 2.2 Related to main text Box 1

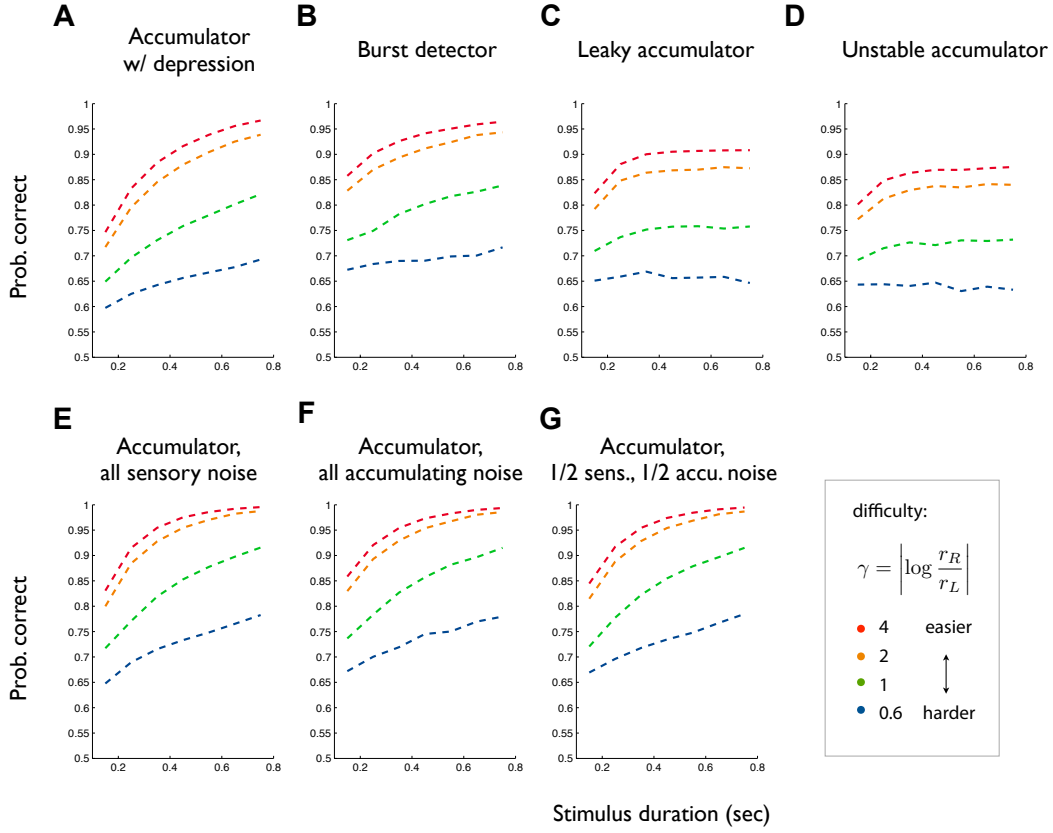
**Choice of sticky bounds and decision rule.** The model described in Box 1 of the main text is an expansion and variation on drift-diffusion type models [3]. Many of those models describe reaction time tasks, in which subjects can report their decision as soon as they feel confident enough to do so. In those models, the decision is reached and reported when the accumulator  $a$  reaches one of the bounds  $B$ . Here we used a controlled-duration task, in which the stimulus duration is controlled by the experimenter [7, 8, 5, 9]. Under these conditions, the question arises, “what should the dynamics be if  $a$  reaches one of the bounds before the ‘Go’ signal is given?”. Kiani et al. [5] have provided evidence that monkeys behave as if the bounds were “sticky”, i.e., reaching a bound represents commitment to a decision that is maintained until the ‘Go’ signal. Behavioral evidence for this proposal has also been found in humans ([10, 8]), which led to our choice of using “sticky” bounds. In addition, there is also the question, “how should the decision be made when  $a$  has not reached a bound when the ‘Go’ signal is given?”. Following refs. [10, 8, 5, 9], the natural choice is to base the decision on the sign of  $a$ .

**Choice of bias term.** Terms representing a leftwards or a rightwards bias in the model can be introduced either at  $t = 0$  (affecting the starting position,  $a(t = 0)$ ), or at the end of the stimulus (affecting the boundary at which the value of  $a$  is divided into leftwards versus rightwards decisions, as described in Box 1 of the main text). Overall, our rats showed very small bias, most likely because during task learning (before data collection), we use automatic methods to penalize biases. The small biases can be seen in the best-fit bias terms (Table 2, Supplementary Information), which are typically less than half a click. We therefore reasoned that two separate bias terms would be unnecessary. To keep the number of parameters to the minimum necessary, we eliminated the starting point bias term, keeping only the bias term at the end of the stimulus.

## 2.3 Related to main text Figure 2

### 2.3.1 Table of best-fit parameters for each individual subject

A table of best-fit parameters and confidence intervals for each individual subject is shown in Table 2.



panel	$\lambda = 1/\tau$	Bound	$\sigma_a^2$	$\sigma_s^2$	$\sigma_i^2$	$\phi$	$\tau_\phi$	bias	lapse
<b>A</b>	0	30	0	70	0	0.34	0.04	0	0
<b>B</b>	-20	4	0	70	0	1	n.a.	0	0
<b>C</b>	-10	30	0	140	0	1	n.a.	0	0
<b>D</b>	+10	30	0	140	0	1	n.a.	0	0
<b>E</b>	0	30	0	140	0	1	n.a.	0	0
<b>F</b>	0	30	140	0	0	1	n.a.	0	0
<b>G</b>	0	30	70	70	0	1	n.a.	0	0

**Fig. S4: Chronometric plots alone do not readily distinguish between widely different decision-making mechanisms.** Chronometric plots as predicted by implementing a variety of strategies show qualitatively similar improvements in performance for longer stimulus durations. Different colors are trials of different difficulties, as defined in the legend. **H** shows the model parameters used to produce the strategies shown in **A-G**. When  $\phi = 1$ , there is no sensory adaptation, so the value of  $\tau_\phi$  is not shown because it is not meaningful.

subject	$\lambda = 1/\tau$	Bound	$\sigma_a^2$	$\sigma_s^2$	$\sigma_i^2$	$\phi$	$\tau_\phi$	bias	lapse rate
rat 052	-0.386 ± 0.195	6-∞	0.0272 ± 0.261	36.6 ± 1.44	0.128 ± 0.129	0.154 ± 0.0387	0.14 ± 0.02	-0.18 ± 0.027	0.094 ± 0.018
rat 053	1.37 ± 0.0595	7-∞	0.00376 ± 0.246	78.2 ± 0.322	1.35e-13 ± 0.0397	0.0843 ± 0.0661	0.065 ± 0.0083	-0.055 ± 0.041	0.016 ± 0.027
rat 065	-0.146 ± 0.342	13-∞	0.00244 ± 1.16	85.8 ± 4.56	3.29 ± 1.23	0.193 ± 0.113	0.022 ± 0.0054	0.047 ± 0.078	0.024 ± 0.01
rat 069	-1.87 ± 0.312	7-∞	1.38 ± 0.243	40.6 ± 1.43	4.72e-05 ± 0.0157	0.351 ± 0.0252	0.067 ± 0.0048	0.25 ± 0.018	0.11 ± 0.01
rat 074	1.02 ± 0.0225	8-∞	4.79e-07 ± 0.0193	49.1 ± 0.0948	0.0897 ± 0.0155	0.252 ± 0.0176	0.044 ± 0.003	-0.15 ± 0.017	0.041 ± 0.0082
rat 083	0.719 ± 0.151	5-∞	0.0045 ± 0.0889	40.2 ± 0.833	2.39e-14 ± 0.0266	0.129 ± 0.0308	0.049 ± 0.0044	-0.067 ± 0.026	0.026 ± 0.009
rat 090	-0.554 ± 0.143	7-∞	0.00106 ± 0.131	58.2 ± 1.18	0.308 ± 0.186	0.136 ± 0.0719	0.065 ± 0.011	0.077 ± 0.028	0.072 ± 0.021
rat 093	-1.24 ± 0.404	6-∞	1.4 ± 0.614	37.5 ± 1.95	0.0567 ± 0.238	0.232 ± 0.0596	0.051 ± 0.009	-0.3 ± 0.057	0.065 ± 0.015
rat 097	-0.662 ± 0.0759	6-∞	5.3e-08 ± 0.0764	36.5 ± 1.46	0.641 ± 0.0731	0.253 ± 0.0325	0.079 ± 0.0051	-0.15 ± 0.016	0.054 ± 0.011
rat 102	1.32 ± 0.288	8-∞	0.000229 ± 0.303	70.8 ± 5.86	2.48 ± 0.281	0.112 ± 0.0357	0.065 ± 0.0072	0.14 ± 0.095	0.066 ± 0.026
rat 103	-1.7 ± 0.395	9-∞	0.407 ± 0.488	66.4 ± 2.74	2.25 ± 0.798	0.0169 ± 0.0349	0.07 ± 0.006	-0.6 ± 0.04	0.054 ± 0.014
rat 104	-0.0486 ± 0.405	10-∞	2.45 ± 4.73	66 ± 11.7	2.98 ± 0.905	0.26 ± 0.0732	0.082 ± 0.011	0.097 ± 0.039	0.12 ± 0.028
rat 105	0.631 ± 0.0432	7-∞	0.143 ± 0.00908	34.6 ± 0.0102	3.71e-14 ± 0.0111	0.101 ± 0.00532	0.084 ± 0.0038	-0.1 ± 0.011	0.06 ± 0.0054
rat 106	-2.32 ± 0.132	8-8	0.363 ± 0.0793	164 ± 0.115	19.8 ± 0.193	0.305 ± 0.00505	0.016 ± 0.0055	1.2 ± 0.011	0.00056 ± 0.028
rat 107	-1.39 ± 0.45	16-∞	0.277 ± 1.84	174 ± 9.06	4.84 ± 1.17	0.197 ± 0.102	0.037 ± 0.0077	-0.47 ± 0.072	7.1e-06 ± 0.018
rat 111	-0.543 ± 0.493	20-∞	13.2 ± 5.38	123 ± 13.7	0.0073 ± 0.383	0.221 ± 0.0915	0.008 ± 0.0036	0.58 ± 0.13	0.056 ± 0.015
rat 112	1.06 ± 0.62	13-∞	4.7 ± 3.29	119 ± 5.26	0.0204 ± 0.504	0.142 ± 0.098	0.047 ± 0.011	-0.96 ± 0.15	0.11 ± 0.027
rat 113	-0.328 ± 0.0273	3-∞	4.87e-09 ± 0.00491	9.74 ± 0.514	4.66e-09 ± 0.00316	0.01 ± 0.00732	0.5 ± 0.014	-8.3e-05 ± 0.0097	0.1 ± 0.01
rat 115	-0.191 ± 0.543	11-13	15.1 ± 5.95	153 ± 12.4	0.949 ± 2.63	0.0758 ± 0.0949	0.034 ± 0.0088	0.13 ± 0.15	0.097 ± 0.043
human D, aud.	-0.116 ± 0.097	16-∞	0.00286 ± 0.472	10.7 ± 1.29	1.7e-08 ± 2.55	0.707 ± 0.118	0.02 ± 0.018	-0.18 ± 0.28	2.8e-09 ± 0.014
human D, vis.	0.0332 ± 0.0344	9-∞	3.27e-10 ± 0.0587	3.43 ± 1.84	0.367 ± 1.48	2.5 ± 0.542	0.1 ± 0.025	-0.41 ± 0.11	1e-07 ± 0.011
human J, aud.	-0.584 ± 0.111	7-7	0.144 ± 0.65	7.69 ± 0.442	2.56 ± 0.495	0.452 ± 0.237	0.02 ± 0.045	-0.79 ± 0.14	3.7e-06 ± 0.24
human J, vis.	-0.0996 ± 0.0168	10-∞	0.0751 ± 0.031	0.373 ± 0.188	1.02e-11 ± 0.125	2.5 ± 0.0787	0.083 ± 0.01	0.12 ± 0.057	1.7e-08 ± 0.0096
human K, vis.	-0.147 ± 0.0346	10-∞	6.4e-05 ± 0.0183	3.51 ± 0.635	5.19e-09 ± 0.301	2.5 ± 0.467	0.078 ± 0.024	-0.35 ± 0.088	0.021 ± 0.025
human R, aud.	-0.304 ± 0.1	13-14	0.378 ± 1.91	11.6 ± 3.69	0.248 ± 3.77	1.03 ± 0.116	0.074 ± 0.12	-0.2 ± 0.26	0.013 ± 0.037
human R, vis.	-0.313 ± 0.131	6-6	0.00142 ± 0.237	2.19 ± 0.575	0.000206 ± 0.227	1.13 ± 0.0514	1 ± 0.26	-0.17 ± 0.058	0.0009 ± 0.041

Table 2: Best-fit model parameters for all subjects, mean ± confidence interval, (confidence interval computation as described in Section 3.5). These values are displayed graphically in Supplementary Figure 5. The values of  $\sigma_s^2$  are expressed in units of clicks<sup>2</sup> per  $N$  incoming pulses, where  $N$  is the mean number of pulses per second for that subject on that task (as specified in Table 2). This convention of units facilitates direct comparison to  $\sigma_a^2$ , which is a diffusion coefficient in units of clicks<sup>2</sup>/sec.

### 2.3.2 Plot of best-fit parameters and confidence intervals for each individual subject

A plot of best-parameters and confidence intervals for each individual subject is shown in Fig. S5. Panels a–f are identical to Fig. 2e–j in the main text, except that rats in each row are uniquely identified by a symbol-color combination, and human subject rows are identified by an initial. In addition, best-fits for parameters not included in Fig. 2 (but described in Box 1),  $\sigma_i^2$ , bias, and lapse rate, are shown here.

Effective adaptation: The net effect of adaptation parameters is strongly dependent on the minimum interpulse interval used in the task. The effective adaptation plotted in Fig. 2g of the main text and here in Fig. S5c is the factor by which the pulse magnitude  $C$  is multiplied following a pulse and the minimum interpulse interval. It thus corresponds to the adaptation actually seen. Letting  $t_{min}$  represent the minimum inter-pulse interval,  $\phi_{\text{effective}}$  is given by

$$\phi_{\text{effective}} = 1 - (1 - \phi) \cdot e^{-t_{min}/\tau\phi} \quad (2)$$

For rats,  $t_{min} = 0$  (see Table 1; details of the stimulus parameters are described in Sections 1.2.1 and 1.2.3). Therefore, for rats  $\phi_{\text{effective}} = \phi$ .



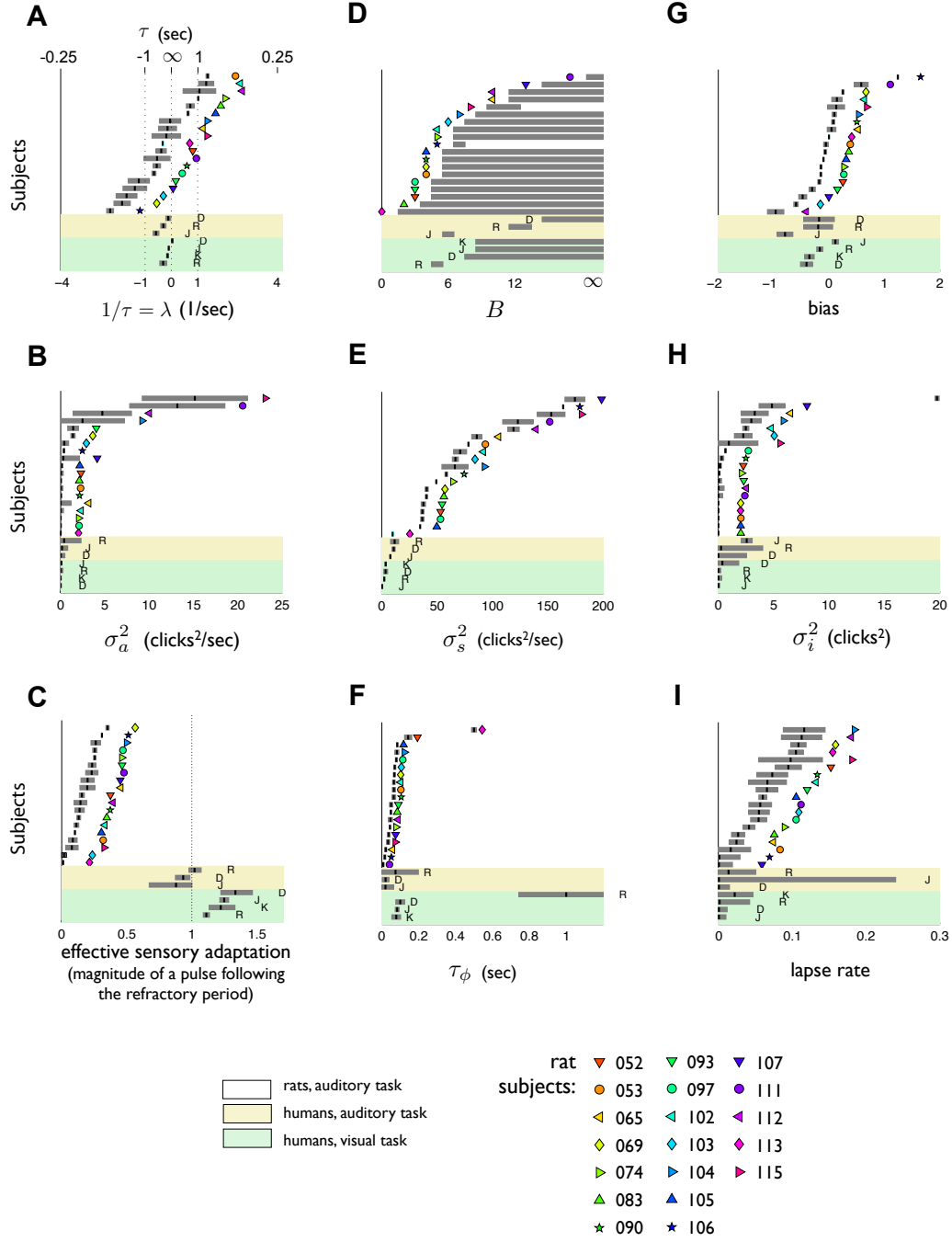


**Fig. S5: Best-fit model parameters for all subjects.** A–F are identical to Fig. 2e–j in the main text, except that rats in each row are uniquely identified by a symbol-color combination (shown in the legend on the bottom right), and human subjects are identified by their initials, to allow comparison of individual subjects across panels.

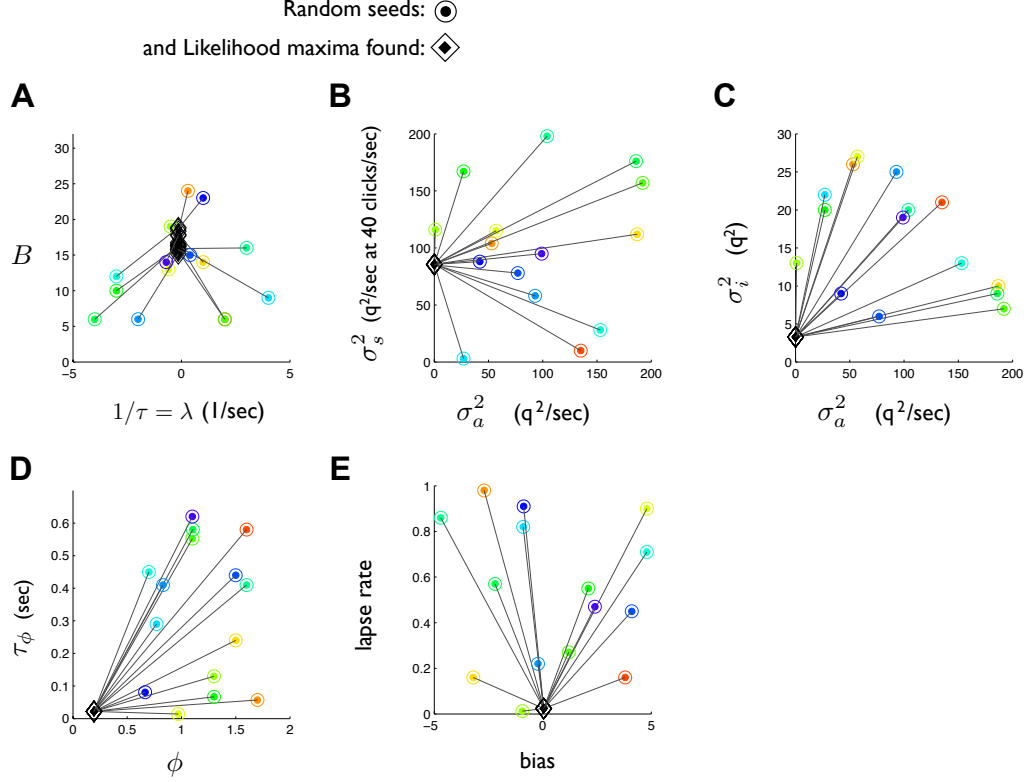


**Fig. S6: The maximum likelihood search finds a single, global maximum.** Random seeds in 8-dimensional parameter space were used in the maximum likelihood search. All searches converged on the same maximum. Each panel shows the projection of the start and end of all searches on each 2-dimensional slice. Searches did not converge on the same value for the Bounds parameter  $B$  because the best-fit likelihood does not change for  $B \geq 12$  (see main text).

### 2.3.3 Model has only one maximum likelihood point in parameter space

As described in the main text, we empirically found only one maximum in parameter space for the likelihood of the model given a subject's data. This observation is consistent with the provably concave log likelihood of a mathematically closely related model, developed to describe the evolution of membrane voltages in single neurons [11]. It suggests that our model may perhaps also be provably concave and have a single maximum.

Fig. S6 shows the result of fitting a single set of data, starting from 20 different randomly chosen points in parameter space. All runs find the same maximum.

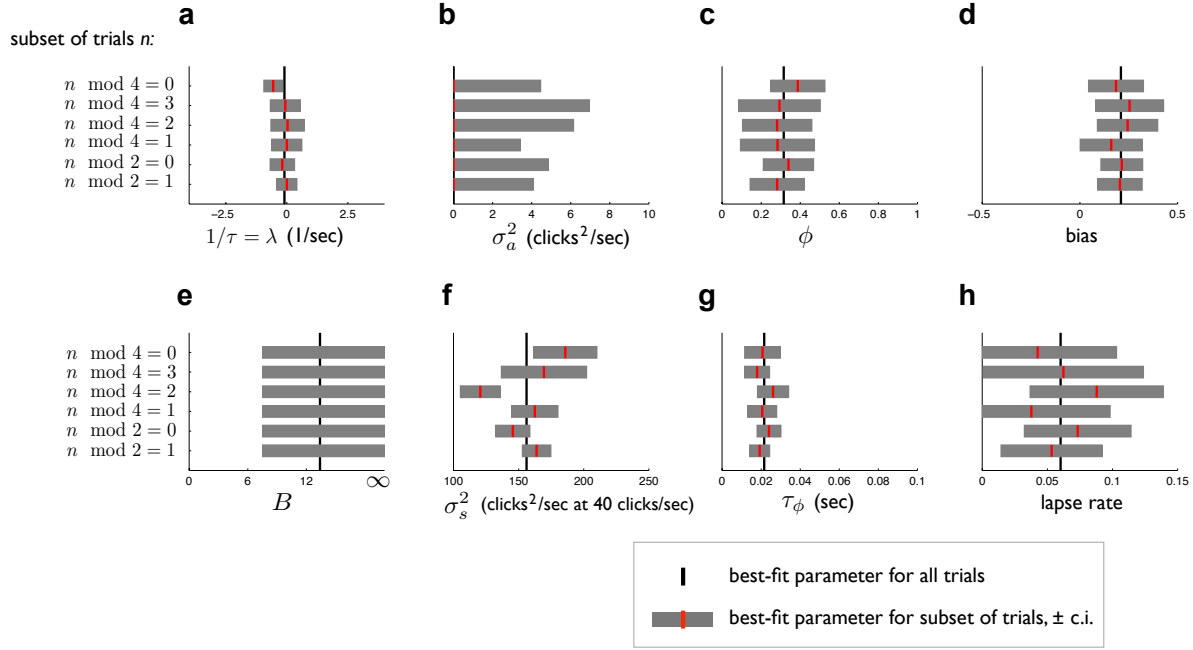


**Fig. S7: Parameter optimization is not sensitive to trial sampling.** Trials for one rat (104, a total of 80423 trials) were subsampled in halves and quarters, then each subset of trials was fit independently. The resultant best-fit parameter values match closely with each other and with the best-fit parameters computed on all trials.

### 2.3.4 Different subsets of data yield identical model fits

Is the model fitting method sensitive to sampling? We repeated the parameter optimization scheme on different subsets of the data for one rat (104). The trials were first broken in half, such that the odd and even trials were fit independently. Next, the trials were broken in quarters (every fourth trial). Fig. S7 summarizes the results of these fits, which match closely with each other and with the best-fit parameters computed on all the trials. Therefore, the fitting method is not over-sensitive to the particular set of trials being sampled.

### 2.3.5 Fitting model-generated data accurately recovers generating parameter values

We generated simulated data using known model parameters, including parameters implementing the different decision-making mechanisms in Fig. S4, then used our optimization scheme to attempt to find the set of parameters best fit to the simulated data. Fifty thousand (50,000) trials were generated using each of 10 different generative parameter sets. The generative parameter sets were chosen to vary each of the 8 model parameters described in Box 1. Fig. S8 shows that our optimization scheme is able to produce best-fit model parameters that closely match the generative parameter values.

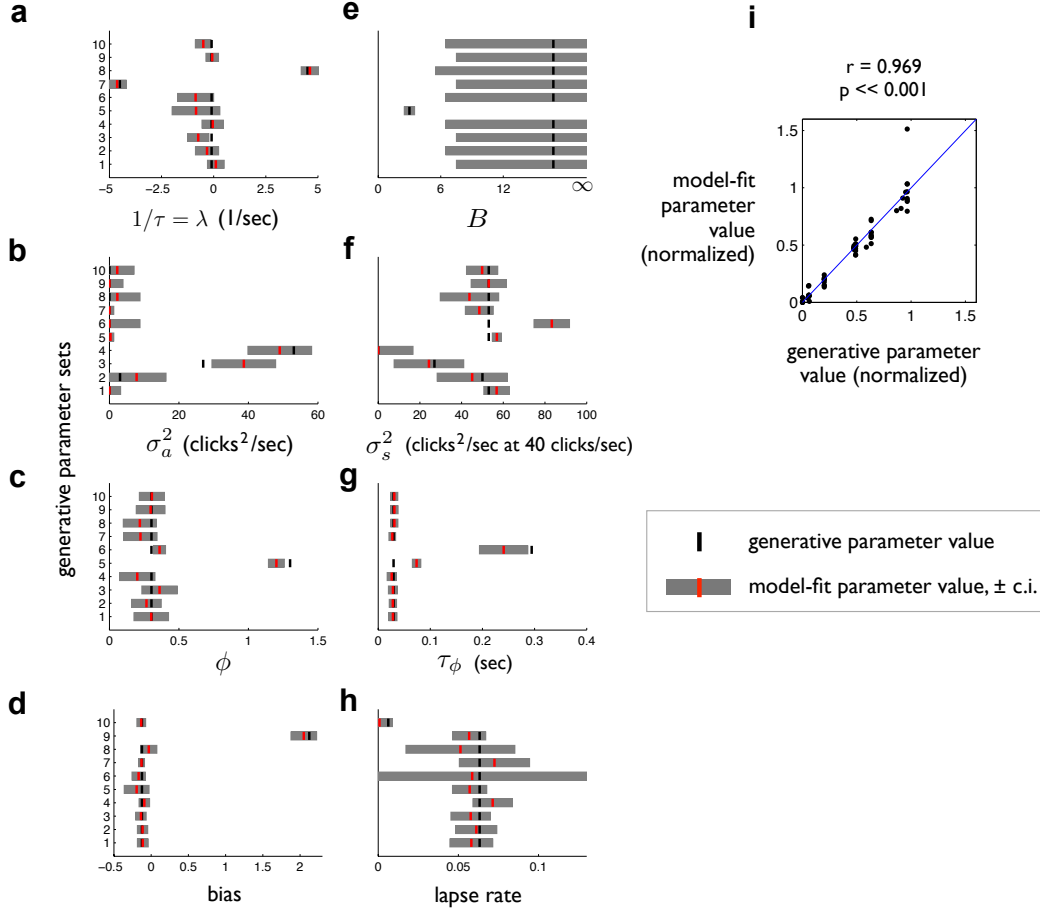


**Fig. S8: The parameter optimization scheme is able to produce best-fit model parameters that closely match the generative parameter values.** a–h, Data was simulated using known, generative parameters (black ticks), and then the parameter optimization scheme described was used to find the model-fit parameter values for the simulated data (red ticks). Ten (10) different generative parameter sets were used in this test, where set  $m$  spans the  $m^{\text{th}}$  row in each panel. Generative parameter sets 1–4 are the same except for the ratio of  $\sigma_a^2$  to  $\sigma_s^2$ ; the optimization scheme is not biased to underestimate the contribution of  $\sigma_a^2$ . i, Summary of the goodness of model-fit parameter values. Parameter values were normalized to enable direct comparison between them.

### 2.3.6 Model fits reliably recover small $\sigma_a^2$ , even in the presence of large $\sigma_s^2$

In the presence of large sensory noise  $\sigma_s^2$ , what is the smallest accumulating noise  $\sigma_a^2$  that can be detected reliably? In other words, if large  $\sigma_s^2$  biased our methods towards under-estimating  $\sigma_a^2$ , how small could  $\sigma_a^2$  be and still be estimated accurately?

We set all model parameters, except for the memory diffusion constant  $\sigma_a^2$ , to their mean value across rats (for the sensory noise  $\sigma_s^2$ , this means that it was set to a large value, 1.67 clicks<sup>2</sup> per incoming click; i.e., at 40 clicks/sec, 67 clicks<sup>2</sup> after one second). We then considered six different values of  $\sigma_a^2$ : [0.001, 0.625, 1.25, 2.5, 5, 10] clicks<sup>2</sup>/sec. For each of these values of  $\sigma_a^2$ , we generated 20 datasets, each of which was generated by running the model on 50,000 trials to generate 50,000 Left-vs-Right choices. We can imagine each of these as the data from a model “rat.” Each of these randomly simulated datasets was then fit with our optimization scheme to find the best-fit parameters (120 model fits in all). Consistent with section 2.3.4, the variability of model-fit values across the 20 datasets for each value of  $\sigma_a^2$  was of a magnitude comparable to computed confidence intervals (Fig. S9C). Fig. S9A shows the median recovered  $\sigma_a^2$  for the different generating  $\sigma_a^2$  values. The unity line is shown in blue. As can be seen, the median recovered  $\sigma_a^2$  closely tracks the generating  $\sigma_a^2$ , across the entire range of values tested.

In the actual experimental data from the rats, 13/19 rats were best fit with  $\sigma_a^2 \approx 0$ . Using our generated data sets, we asked how small the generating  $\sigma_a^2$  would have to be to produce 13/19 datasets with a recovered  $\sigma_a^2$  close to zero. Here we defined “close to zero” as  $\sigma_a^2 < 0.5$ . Fig. S9b shows the results.  $\sigma_a^2$  had to be smaller than 0.625 clicks<sup>2</sup>/sec to produce 13/19 or more datasets with a recovered  $\sigma_a^2 < 0.5$ . Thus, even with large sensory noise  $\sigma_s^2$ , we can place an upper bound on  $\sigma_a^2$  of 0.625 clicks<sup>2</sup>/sec.

### 2.3.7 A restricted model where $\sigma_a^2 = 0$ and $B \rightarrow \infty$ is favored by AIC analysis

To confirm further results from fitting the full 9-parameter model that  $\sigma_a^2$  is zero and  $B$  is very large, we fit the data to a restricted, 7-parameter model where  $\sigma_a^2 = 0$  and  $B \rightarrow \infty$ . Table 3 shows an AIC analysis of the best fits under these two alternate models favored this 7-parameter model for 15/19 rats and 5/7 humans.

### 2.3.8 Aspects of the data not well fit by the model

Although the model fits the data very well, there are two aspects that it does not fit well, and that could be better captured in future model refinements. First, performance at high stimulus difficulties (low values of  $\gamma$ ) tends to decrease at the longest stimulus durations (Fig. S3). Slowly collapsing bounds could perhaps capture this aspect. Second, the psychophysical reverse correlation at the very beginning of the stimulus tends to be slightly less separated in the data than in the best-fit model predictions (Fig. S10). Although this effect is very weak, it is consistent across rats.

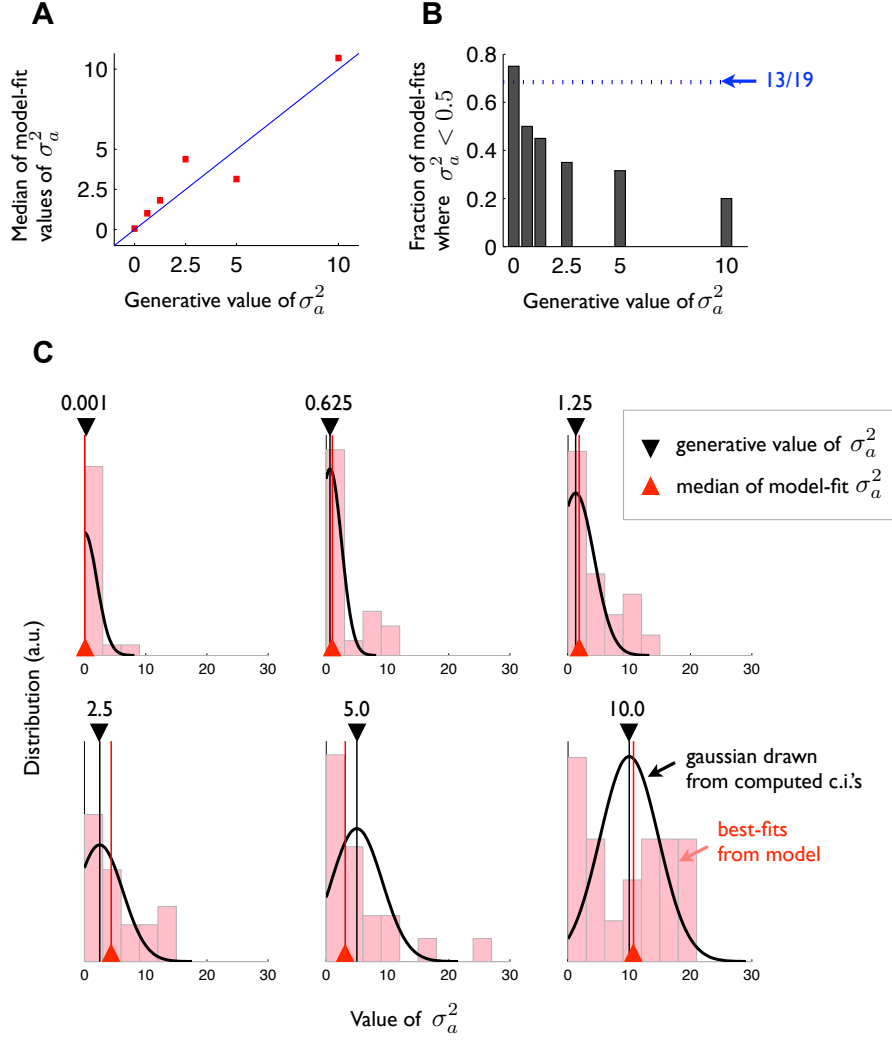


**Fig. S9: Model fits reliably recover small  $\sigma_a^2$ .** Multiple randomly simulated datasets were generated based on known values of  $\sigma_a^2$  (all other parameters held fixed,  $\sigma_s^2$  set to 1.67 clicks<sup>2</sup> per incoming click), and the best-fit parameter values were computed for each dataset. **A** shows that the median of model-fit values of  $\sigma_a^2$  close approximates each known, generative  $\sigma_a^2$ . **B**, To match or exceed the fraction of datasets best-fit by  $\sigma_a^2 \approx 0$  in the experimental rat data (13/19), the true, underlying  $\sigma_a^2$  must be smaller than 0.625 clicks<sup>2</sup>/sec. **C**, the variability of model-fit values (distribution in pink) was comparable in magnitude to computed confidence intervals (gaussian drawn in black).

subject	LL of 9-param model	LL of 7-param model	AIC of 9-param model	AIC of 7-param model	difference of AIC's
rat 052	-22978.9	-22978.9	45975.9	45971.9	4.00
rat 053	-15477.8	-15477.8	30973.6	30969.7	3.90
rat 065	-11880.4	-11880.4	23778.7	23774.8	3.93
rat 069	-28684.0	-28692.4	57385.9	57398.7	-12.78
rat 074	-41542.5	-41543.1	83103.0	83100.2	2.76
rat 083	-16792.0	-16792.0	33601.9	33597.9	3.97
rat 090	-29886.9	-29887.0	59791.8	59788.0	3.77
rat 093	-20555.5	-20556.9	41128.9	41127.8	1.14
rat 097	-32411.1	-32411.6	64840.2	64837.1	3.11
rat 102	-22858.4	-22858.4	45734.8	45730.9	3.88
rat 103	-25714.3	-25715.4	51446.6	51444.8	1.77
rat 104	-41743.3	-41795.1	83504.6	83604.1	-99.48
rat 105	-22301.2	-22301.7	44620.4	44617.3	3.11
rat 106	-29645.1	-29677.6	59308.1	59369.2	-61.11
rat 107	-21685.1	-21685.4	43388.3	43384.8	3.50
rat 111	-9953.3	-9955.9	19924.6	19925.8	-1.25
rat 112	-9662.5	-9662.7	19342.9	19339.5	3.49
rat 113	-10587.2	-10589.2	21192.4	21192.3	0.08
rat 115	-10595.8	-10596.3	21209.6	21206.6	3.05
human D, aud.	-890.1	-890.1	1798.1	1794.1	3.98
human D, vis.	-498.5	-498.6	1014.9	1011.2	3.75
human J, aud.	-736.8	-747.9	1491.6	1509.8	-18.22
human J, vis.	-453.6	-453.8	925.2	921.7	3.49
human K, vis.	-999.0	-999.5	2016.1	2012.9	3.15
human R, aud.	-942.9	-943.0	1903.8	1900.1	3.71
human R, vis.	-1059.6	-1065.7	2137.2	2145.3	-8.10

Table 3: A comparison of the log-likelihood (LL) of fits under the full, 9-parameter model and a restricted, 7-parameter model where  $\sigma_a^2 = 0$  and  $B \rightarrow \infty$ . An AIC analysis favored the 7-parameter model in 15/19 rats and 5/7 humans, confirming the observation that  $\sigma_a^2$  is small and  $B$  is large.

## 2.4 Related to main text Figure 3

### 2.4.1 Result of model-free analyses for each individual subject

The best-fit, maximum likelihood model obtained makes several predictions about structure that should be present in the behavioral data. We undertook a series of model-free analyses, both to confirm these predictions and to compare directly the magnitude of each effect. Figure 3a,c shows these model-free analyses for an example rat (065) and Fig. S10 contains the same analyses for all 19 subjects.

Fig. S11 summarizes the burstiness analysis for all rats. Performance was significantly worse on bursty trials for 16/19 rats (see Section 4.2 for methods). None of the humans showed a significant difference in performance between bursty and non-bursty trials.

Detailed methods on model-free analyses are found in Section 4.



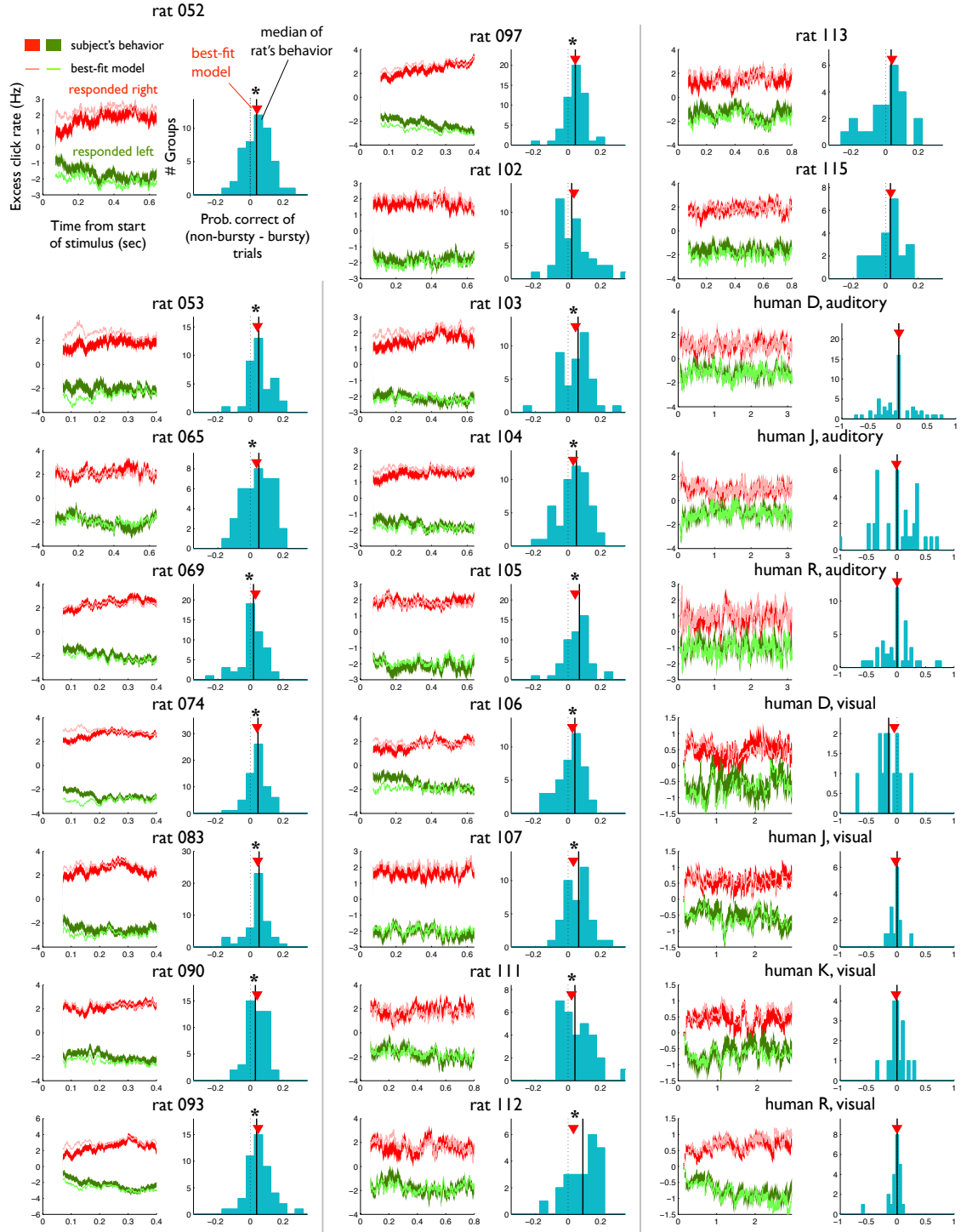


**Fig. S10:** A summary of model-free analyses for all subjects, as described in section 4. Each set of two panels is identical to what was shown in Fig. 3a and 3c for one rat (065). On the right side panels, an asterisk denotes that there was a significant ( $p < 0.05$ ) improvement in performance on non-bursty versus bursty trials.

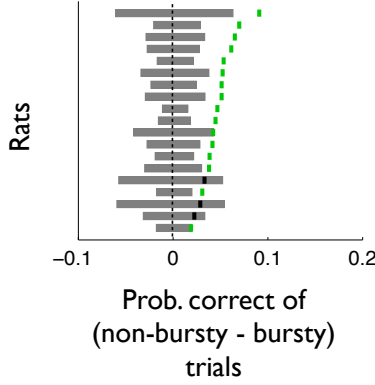


**Fig. S11: Summary of the burstiness analysis for all rats.** The green marks indicate, for each rat, the median improvement in performance of non-bursty versus bursty trials, as defined in section 4.2. The grey bars show the 95% confidence intervals of the bootstrapped, shuffled medians. Light green ticks are significant ( $p < 0.05$ ) improvements, and dark green ticks are not significant.

#### 2.4.2 Performance on single-click difference trials is well predicted by model fit to multi-click trials

The sensory noise parameter  $\sigma_s^2$  represents noise induced in the accumulator by a single pulse of sensory evidence. On short duration trials where there is only a single click from one side, the sensory noise  $\sigma_s^2$ , together with the variance in the initial conditions  $\sigma_i^2$ , will almost entirely determine performance. This is because on short trials both the  $\lambda$  term and the  $\sigma_a^2$  term will have negligible effect; and on trials with only one side click, the adaptation parameters have no effect on how much probability mass is found on each side of the decision boundary  $a = 0$ . Performance on short duration trials with only one side click thus allow us to directly assess our estimates of  $\sigma_s^2$  and  $\sigma_i^2$ . Note that best-fit values for  $\sigma_i^2$  were zero or very small for a majority of the subjects (Fig. S5h). This analysis therefore mostly focuses on  $\sigma_s^2$ .

We looked at the rats' performance on trials where there was one extra click on one side, so that  $|N_R - N_L| = 1$  and  $N_R + N_L = 3$ ; because of the first, stereo click in the rats' auditory task (Methods 1.2.1), there was always at least one click on each side. This subset of trials were presented about 0.5% of all trials and were 120 msec in duration on average. Trials of this type were not present in the human auditory task, which had a much longer range of durations (2-4 sec). But we did find a sufficient number of these  $|N_R - N_L| = 1$  and  $N_R + N_L = 3$  trials in the human visual task to allow the analysis.

For each subject, the model was fit to the set of trials where  $|N_R - N_L| > 1$ , and these alternate best-fit model parameters were used to predict performance on the omitted  $|N_R - N_L| = 1$  and  $N_R + N_L = 3$  trials. As shown in Figure 3b, the predicted performance was accurate on a subject-by-subject basis.

#### 2.4.3 The data sharply constrains the model-fit total variance

Figure 3b suggests that  $\sigma_i^2$  and  $\sigma_s^2$  were estimated accurately. If the sum of the three types of variances  $\sigma_a^2 + \sigma_s^2 + \sigma_i^2$  is also well constrained by the data, then  $\sigma_a^2$  is estimated accurately as well. Fig. S12 shows

the normalized likelihood of the model as the fits diverge from the best-fit parameters. For this analysis, all parameters except the three  $\sigma$ 's were held at their best-fit values, and distance was measured as linear distance in  $(\sigma_a^2, \sigma_s^2, \sigma_i^2)$  space normal to the plane defined by  $\sigma_a^2 + \sigma_s^2 + \sigma_i^2 = \text{sum of their best-fit values}$ . This likelihood drops off sharply away from the point of best-fit, suggesting the total variance fit by the model is well constrained by the data.

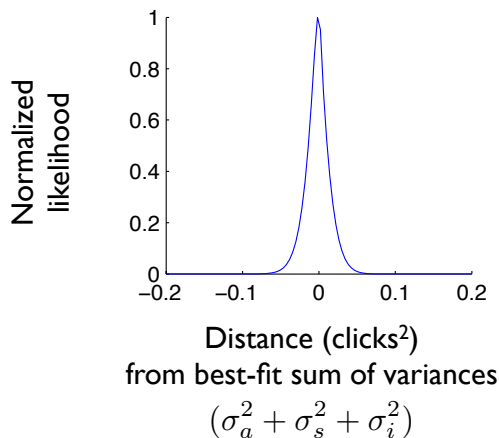


**Fig. S12:** The data sharply constrains the model-fit total variance.

#### 2.4.4 Testing $\sigma_a^2 = 0$ : Relative accuracy improved on trials with relatively longer stimulus durations.

We reasoned that if the memory diffusion noise  $\sigma^2$  is large, then longer stimulus durations should lead to greater variance due to diffusion, and thus to reduced performance. To assess whether performance was indeed reduced at longer durations, while controlling for the amount of sensory evidence and sensory noise provided, we subdivided trials into different groups, where trials within each group all had equal sensory evidence and total single-pulse noise, but could have different stimulus durations. Each group was labelled by a pair  $[N_R, N_L]$  and was composed of all those trials that had  $N_R$  right clicks and  $N_L$  left clicks. As described above, if  $\sigma_a^2$  is large, longer durations would lead to greater accumulation of diffusion noise, and performance within a group should decay with duration. In contrast, if  $\sigma_a^2 \approx 0$ , performance should not depend on stimulus duration and should therefore stay constant. However, instead of these two possibilities the rat data (Fig. S13, black dots) showed significant increase in performance with stimulus duration (Fig. S13)<sup>1</sup>. This increase is explained by the presence of click depression: trials with longer stimulus durations within each group tend to have longer intervals between clicks, thus reducing the impact of click depression and improving performance. Indeed, model predictions with  $\sigma_a^2 \approx 0$  plus the presence of click depression matched the data very well (Fig. S13, red lines).

<sup>1</sup>There were insufficient numbers of trials in the human data to perform the same analysis

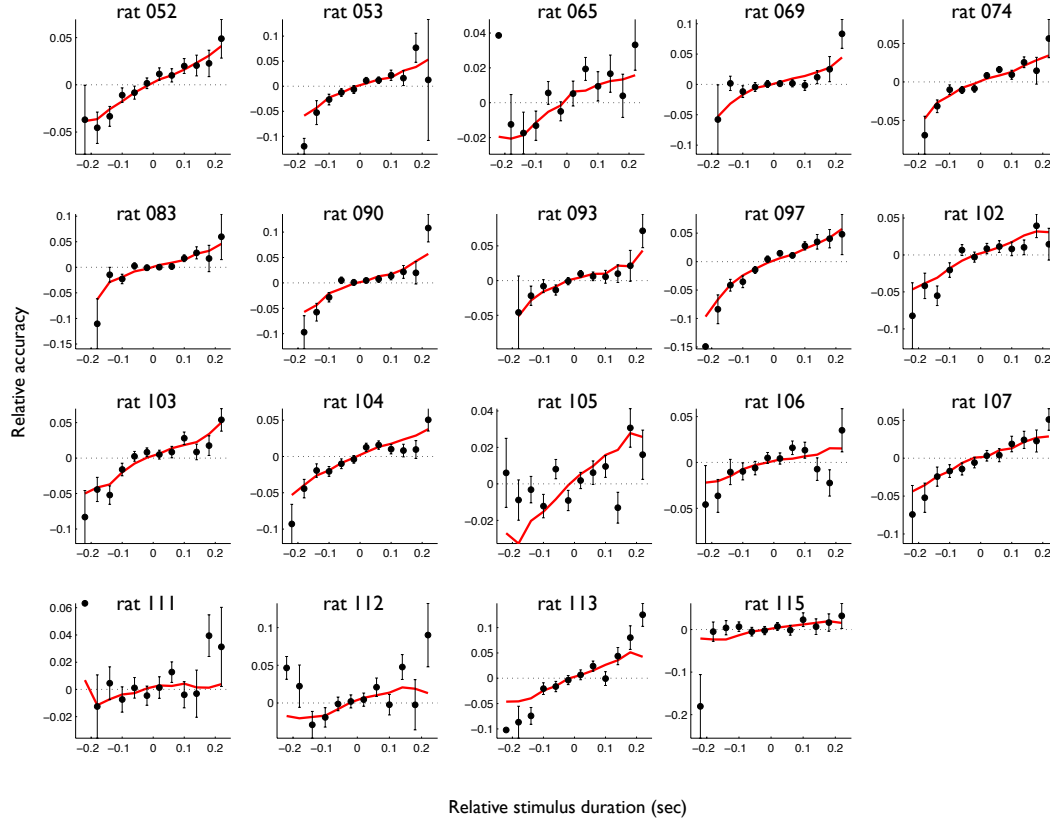


**Fig. S13: When trials were grouped such that sensory evidence was held constant, relative accuracy improved on trials with relatively longer stimulus durations.** The black dots are the rats' behavioral data (mean  $\pm$  s.e.m.). The red line is predicted by the best-fit parameters for each rat. This observation is consistent with  $\sigma_a^2 \approx 0$  and the presence of click depression.

### 3 Modeling Methods

To evaluate how well a particular set of parameter values  $\theta$  fits the behavioral data, we compute the probability of observing the data given the model. In this methods section, we refer to each pulse of evidence as a left or right click, but each pulse of evidence may also be a flash of left or right oriented bar, as in the visual version of the task the human subjects performed.

Let  $t_{i,R}$  and  $t_{i,L}$  represent the right and left click times on trial  $i$ , let  $d_i$  represent the subject's decision on trial  $i$ , and let  $D$  represent the full set of the subject's decisions across all trials. Assuming that trials are independent, we may compute the likelihood of seeing the data under the model:

$$P(D|\theta) = \prod_i P(d_i|t_{i,R}, t_{i,L}, \theta) \quad (3)$$

The best-fit parameter values (also known as the maximum likelihood values) are the parameters  $\theta$  that maximize equation (3). Since the logarithm is a monotonic function, these are also the parameters that maximize the log likelihood:

$$\ln P(D|\theta) = \sum_i \ln P(d_i|t_{i,R}, t_{i,L}, \theta) \quad (4)$$

We work with either equation (3) or equation (4), according to which is more convenient.

Below we first describe, in section 3.1, how we compute  $P(d_i|t_{i,R}, t_{i,L}, \theta)$  for each trial. Then, to help us maximize equation (4), we developed methods to compute the derivative  $\partial \ln P(d_i|t_{i,R}, t_{i,L}, \theta) / \partial \theta$  for each of the parameters in the set  $\theta$ . These methods are described in section 3.2. Section 3.3 describes the specifics of how these gradient computation methods were applied to the 9 model parameters of the model. Using this gradient information, we then applied standard optimization methods described in section 3.4. Finally, methods to obtain confidence intervals on the optimal parameter values  $\theta$  are described in section 3.5.

#### 3.1 Computing the probability of a response given a trial's model parameters and click times

Box 1 of the main text describes the model and the dynamical equations for the decision variable  $a$ . These equations are reproduced here:

$$da = \begin{cases} 0 & \text{if } |a| \geq B; \\ \sigma_a dW + (\delta_{t,t_R} \cdot \eta C(t) - \delta_{t,t_L} \cdot \eta C(t)) dt + \lambda a dt & \text{otherwise.} \end{cases} \quad (5)$$

where

$\delta_{t,t_{R,L}}$  are delta functions at the times of the clicks

$\eta$  are i.i.d. gaussian variables drawn from  $\mathcal{N}(1, \sigma_s)$

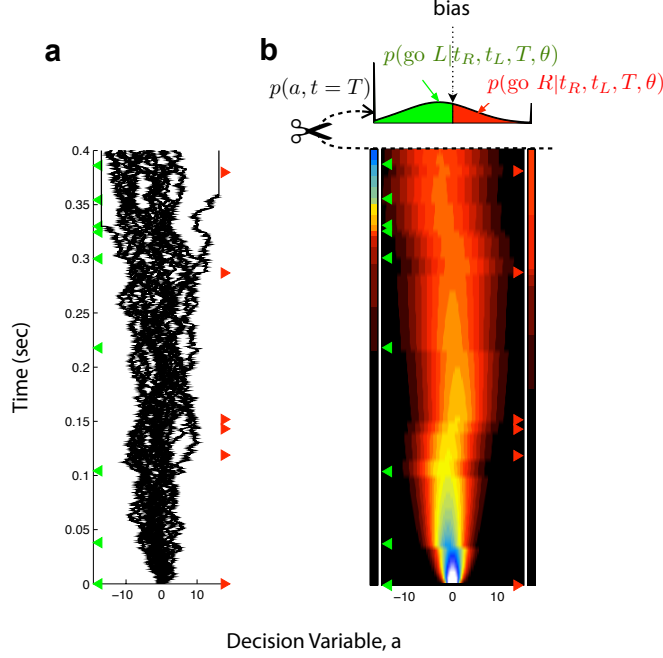


**Fig. S14: Evaluating the probability of a Left-vs-Right response given model parameters and click times for a single trial.** Green and red triangles mark the timing of left and red clicks, respectively. **a**, The plot shows the evolution of the decision variable  $a$  over time, as governed by equation (5). Each black line is a possible path for the decision variable  $a$ ; different lines are produced by different instantiations of the noise variables. **b**, A heat map illustrating the temporal evolution of a probability distribution over possible values of the decision variable  $a$ , for the same model parameter values and click times as shown in panel **a**. This distribution is identical to one obtained by computing an large number of individual possible paths as done in **a**. However, evolving the probability distribution directly is much more computationally efficient than evolving thousands of individual paths. Notice that at timepoints where a left or right click was played, the entire distribution shifts left or right. The total variance of the distribution increases with time in between clicks, since in this example the accumulating noise  $\sigma_a^2 > 0$ . The leftmost and rightmost bins represent the sticky bounds, and the white space drawn between them and the rest of  $a$  space emphasizes the property that probability can flow into but not out of those bins. At the end of the stimulus duration, the distribution of  $a$  (top,  $p(a, t = T)$ ) is used to evaluate the probability of the model producing a left or a right response in this trial. The area under the curve to the left (right) of the bias threshold is the probability of the model producing a left (right) response.

$dW$  is a white noise Wiener process.

The initial condition for this dynamical equation at  $t = 0$ , defined to be the time of the first stereo click, is the gaussian distribution  $\mathcal{N}(0, \sigma_i)$ .

The impact of each click ( $C$ ) is affected by sensory adaptation that depends on clicks from both right and left sides:

$$\frac{dC}{dt} = \frac{1 - C}{\tau_\phi} + (\phi - 1)C(\delta_{t, t_R} + \delta_{t, t_L}) \quad (6)$$

In addition, if a stereo click (simultaneous clicks on left and right) is played, the clicks cancel and  $C = 0$ . In other words, a stereo click played at  $t = 0$  of a trial means that  $C(t = 0) = 0$ .

Let us define a unit of evidence called “q” corresponding to the magnitude of one click in the absence of sensory adaptation ( $\phi = 1$ ). An ideal observer adds one q at every right click and subtracts one q at every left click. It is worth noting that variance due to incoming sensory evidence  $\sigma_s^2$  is expressed in units of  $q^2$  for each incoming click. However, to facilitate direct comparison with the magnitude of  $\sigma_a^2$ , which is a diffusion coefficient with units of  $q^2/\text{sec}$ , we sometimes express the value of  $\sigma_s^2$  in units of  $q^2/\text{sec}$  for  $N$  clicks/sec, where  $N$  is fixed for each subject in each task (e.g., in main text Fig. 2, Fig. S5, and Table 2). For the rats’ auditory task,  $N = 40$  clicks/sec; for the humans’ auditory task,  $N = 20$  clicks/sec; for human subjects D, J, and K on the visual task,  $N = 4.5$  pulses/sec; and for human subject R on the visual task,  $N = 3$  pulses/sec.

The form of the model in (5) is that of a generalized Ornstein-Uhlenbeck (OU) stochastic process. The evolution of  $a$  on each trial is a function of the parameter values and of the specific times of left and right clicks played. Because of the stochastic nature of the model (i.e., the noise terms in the model,  $\sigma_a^2$ ,  $\sigma_s^2$  and  $\sigma_i^2$ ), multiple identical runs of the model, with the same parameters and click times but with different instantiations of the noise variables, will lead to different traces of  $a$  over time (Fig. S14a).

Given a set of model parameter values ( $\theta$ ) and click times for a particular trial ( $\{t_i\}$ ), we seek to evaluate  $P(d = L|\theta, \{t_i\})$ , the probability that the model would produce a “Left” decision. Because this is a two-alternative forced-choice task, the probability of a “Right” decision is also obtained as  $P(d = R) = 1 - P(d = L)$ . We could evaluate the desired probability simply by evolving equation (5) many different times, as shown in Fig. S14a, and finding which fraction of times the final value of  $a > \text{bias}$ . A much faster and equivalent computation is to work directly in probability space, and compute  $P(a, t)$ , the probability distribution of  $a$  at each point in time. We then obtain the probability of going left from

$$P(d = L|\theta, \{t_i\}) = \int_{a=-\infty}^{\text{bias}} da P(a, T|\theta, \{t_i\}) \quad (7)$$

where  $T$  is time at the end of the stimulus. Computing  $P(a, t)$  requires solving the Fokker-Planck equations that correspond to equation (5).

If there were no sticky (i.e., absorbing) decision bounds  $B$ , we could use analytical solutions for  $P(a, t)$  [12]. However, the bounds preclude this. Instead, we will solve the Fokker-Planck equations numerically.



To do this, we discretize both time  $t$  and space  $a$ , and start with the distribution at time  $t = 0$ , which we set to be a gaussian with mean zero  $P(a, t = 0) = \mathcal{N}(0, \sigma_i)$ . (If  $\sigma_i = 0$ , then the initial distribution becomes a delta function at  $a = 0$ .) We then compute the probability distribution for the next time step given the probability distribution for the previous timestep, and iterate through timesteps until  $t = T$ .

### 3.1.1 The forward transition matrix for the discretized Fokker-Planck system

We discretize time into steps indexed by  $k$ , such that  $a_k$  represents the value of  $a$  at timestep  $k$ . We also discretize the possible values of  $a$  into a set of  $M$  contiguous bins; let us define a vector  $\xi$  whose elements represent the positions of the different  $a$  bins that we are using. We will use the indices  $i$  and  $j$  to indicate our spatial bins. For example, then, bin  $i$  has its center at position  $\xi_i$ . The evolution of the probability  $P(a, t)$  from timestep  $k - 1$  to timestep  $k$  is then defined by the forward Markov transition matrix  $F$ :

$$F_{ij} = P(a_k = \xi_i | a_{k-1} = \xi_j). \quad (8)$$

If  $f_k$  represents the spatially discretized version of the distribution  $P(a, t_k)$ , we have

$$f_k = F f_{k-1} \quad (9)$$

Iterating equation (9) allows us to find  $P(a, T)$  starting from  $P(a, 0)$ . Before we consider how  $F_{ij}$  is determined in our model, let us briefly consider the general problem of how to evolve the first moment of distributions accurately when space has been discretized.

#### 3.1.1.1 Exact preservation of the evolution of the first moment of the distribution.

Consider the following problem. Let us imagine that the our continuous-time and continuous-space equations for the evolution of the probability  $P(a, t)$  tell us that at some point in time  $t = t_k$ , all the probability mass should be placed at position  $a = s$ ; that is,  $P(a, t_k) = \delta(a - s)$ . However, given that we have discretized space, how should we represent this if  $s$  is not at the center of one of our spatial bins? We can exactly preserve the first moment of the distribution using a scheme in which probabilities are “settled” in proportion to their proximities to the two closest bin centers<sup>2</sup>. Specifically, when  $s$  falls in between bins at  $\xi_i$  and  $\xi_{i+1}$ , let the probability mass be divided into its two nearest bins such that

$$\begin{aligned} P(a_k = \xi_i) &= \frac{\xi_{i+1} - s}{\xi_{i+1} - \xi_i} \\ P(a_k = \xi_{i+1}) &= \frac{s - \xi_i}{\xi_{i+1} - \xi_i} \\ \implies \langle a_k \rangle &= \xi_i P(a_k = \xi_i) + \xi_{i+1} P(a_k = \xi_{i+1}) = s. \end{aligned} \quad (10)$$

As shown in equation (10), this method of discretization exactly preserves  $\langle a_k \rangle$ , the first moment of the distribution with zero error (but not necessarily the second moment), regardless of the size of the spatial bins or of the timestep  $dt$ . The approach in equation (10) allows exact evolution of the first moment of the distribution even when  $\sigma_a^2 \rightarrow 0$  and timesteps and spatial bins are large.

---

<sup>2</sup>We are indebted to J.J. Hopfield for this method.

### 3.1.1.2 Determining $F_{ij}$ , the forward Markov transition matrix

The equation defining the dynamics of our OU process is the standard

$$da = (\lambda a + c)dt + \sigma dW \quad (11)$$

where  $c(t) = (\delta_{t,t_R} \cdot \eta C(t) - \delta_{t,t_L} \cdot \eta C(t))$ . Here  $\lambda$  is the deterministic (advective) term,  $c$  is the input to the system that will be considered as constant for each  $dt$ , and  $dW$  is the white noise, Wiener process. Let us assume that we are integrating the corresponding Fokker-Planck equations over a small timestep  $dt$ . Then solving the deterministic portion of the equations tells us that if at timestep  $k-1$  the decision variable  $a$  had value  $a_{k-1}$  then, on average at timestep  $k$ ,

$$\mu = a_k = \exp^{\lambda dt} \left( a_{k-1} + \frac{c}{\lambda} \right) - \frac{c}{\lambda} \quad (12)$$

In addition to the deterministic forward propagation, the Wiener process tells us to expect Gaussian dispersion with variance  $\sigma^2 dt$ . We thus get the following Markov forward propagation term with Gaussian form:

$$P(a = a_k | a = a_{k-1}, \theta) = \frac{1}{\sqrt{2\pi\sigma^2 dt}} \exp \left( -\frac{(a_k - \mu)^2}{2\sigma^2 dt} \right) \quad (13)$$

To implement this propagation according to the discretization scheme as described above in section 3.1.1.1, it will be convenient to represent the Gaussian distribution of equation (13) in a discretized form where the bin sizes are much smaller than  $\sqrt{\sigma^2 dt}$ , in order to allow faithful representation of the diffusive process. (Note that the discretization of this Gaussian is done with bins different to the  $\xi$  vector used to discretize the space  $a$ .)

For each bin  $\xi_j$ , let's define  $\mu_j$  following equation (12), and use that to define the continuous function of  $s_j$ :

$$p(s_j) = \frac{1}{\sqrt{2\pi\sigma^2 dt}} \exp \left( -\frac{(s_j - \mu_j)^2}{2\sigma^2 dt} \right) \quad (14)$$

We then discretize  $s_j$  using spatial bins much smaller than  $\sqrt{\sigma^2 dt}$ , with bins extending at least  $4\sqrt{\sigma^2 dt}$  on each side of  $\mu_j$ . Finally, we “settle” the probability mass for each  $s_j$  bin into one of the  $\xi$  bins, following the prescription of Section 3.1.1.1. Thus, each element in  $p(s_j)$  is settled into the closest bins  $\xi_i$  and  $\xi_{i+1}$ , so that  $F_{i,j}$  is a sum over all the bins of  $p(s_j)$  whose positions  $s_j$  fall between  $\xi_{i-1}$  and  $\xi_{i+1}$ , weighted by the relative distances between  $\xi_i$  and  $s_j$ :

$$F_{i,j} = \sum_{\xi_i < s_j < \xi_{i+1}} p(s_j) \frac{\xi_{i+1} - s_j}{\xi_{i+1} - \xi_i} + \sum_{\xi_{i-1} < s_j < \xi_i} p(s_j) \frac{s_j - \xi_{i-1}}{\xi_i - \xi_{i-1}} \quad (15)$$

$$F_{i+1,j} = \sum_{\xi_i < s_j < \xi_{i+1}} p(s_j) \frac{s_j - \xi_i}{\xi_{i+1} - \xi_i} + \sum_{\xi_{i+1} < s_j < \xi_{i+2}} p(s_j) \frac{\xi_{i+2} - s_j}{\xi_{i+2} - \xi_{i+1}} \quad (16)$$

### 3.2 The gradient of the log likelihood of the model fit

Our numerical approach to computing the gradient  $\partial P(d_i|t_{i,R}, t_{i,L}, \theta)/\partial \theta$  is indebted to M. Nikitchenko & L. Paninski. These authors' methods are in turn based on Salakhutdinov, Roweis, & Ghahramani [13]. This last is a paper written with a machine learning audience in mind. We wish to make these methods accessible to a general neuroscience audience. As a consequence, below we describe in full all the steps necessary to obtain the gradient. Most of the description of these methods, then, does not concern novel material.

The main novel feature that is developed here, for the purpose of computing the gradient of model likelihood, concerns the case where the bounds of the OU model are sticky — hitting the bound corresponds to committing to a decision. The position of the bounds is a parameter, so we must compute the derivative with respect to the position of the bounds.

#### 3.2.1 Gradient of the log likelihood of a model with hidden variables

We begin by considering the general case of a probabilistic generative model that has parameters  $\theta$  and produces outputs  $d$  with probability  $P(d|\theta)$ . Let us further assume that the output  $d$  depends only on some hidden variables  $a$ , such that  $P(d|a, \theta) = P(d|a)$ . Then

$$\begin{aligned}
\frac{\partial \ln P(d|\theta)}{\partial \theta} &= \frac{1}{P(d|\theta)} \frac{\partial P(d|\theta)}{\partial \theta} = \frac{1}{P(d|\theta)} \frac{\partial}{\partial \theta} \int P(d, a|\theta) da \\
&= \int \frac{1}{P(d|\theta)} \frac{P(d, a|\theta)}{P(d, a|\theta)} \frac{\partial}{\partial \theta} P(d, a|\theta) da \\
&= \int P(a|d, \theta) \frac{\partial}{\partial \theta} \ln P(d, a|\theta) da = \int P(a|d, \theta) \frac{\partial}{\partial \theta} \ln [P(d|a, \theta) P(a|\theta)] da \\
&= \int P(a|d, \theta) \frac{\partial}{\partial \theta} [\ln P(d|a, \theta) + \ln P(a|\theta)] da = \int P(a|d, \theta) \frac{\partial}{\partial \theta} [\ln P(d|a) + \ln P(a|\theta)] da \\
&= \int P(a|d, \theta) \frac{\partial}{\partial \theta} \ln P(a|\theta) da
\end{aligned} \tag{17}$$

That is, we take the derivative of the log prior probability of the hidden variables  $P(a|\theta)$ , weight that by the posterior probability of the hidden variables  $P(a|d, \theta)$ , and integrate. Sometimes it will be convenient to write the derivative as in (17); other times we'll find it convenient to write it as

$$\frac{\partial \ln P(d|\theta)}{\partial \theta} = \frac{\partial}{\partial \theta} \int P(a|d, \hat{\theta}) \ln P(a|\theta) da \tag{18}$$

where  $\hat{\theta} = \theta$ , but is written with the hat symbol to indicate that the derivative w.r.t.  $\theta$  will not apply to it.

### 3.2.2 When the hidden variables are a Markov process

We'll now assume further structure in the vector of hidden variables  $a$ . We'll assume that these variables are a first-order Markov process, so that each one depends only on its predecessor:

$$P(a_k|a_1, a_2, \dots, a_{k-1}, \theta) = P(a_k|a_{k-1}, \theta) \quad (19)$$

(If we are discretizing space (as we do for numerical Fokker-Planck simulations), and the different indices  $k$  represent different timepoints, then  $P(a_k|a_{k-1}, \theta)$  is the Markov transition matrix for the timestep from time  $k - 1$  to time  $k$ .)

In this Markov case, the posterior weighting term  $P(a|d, \theta)$  represents the probability distribution of all *paths through time* that end up producing the output  $d$ . The probability distribution  $P(a|\theta)$  factorizes into products of the Markov matrices:

$$P(a|\theta) = P(a_1, a_2, \dots, a_N|\theta) = P(a_1|\theta)P(a_2|a_1, \theta)P(a_3|a_2, \theta)\dots P(a_N|a_{N-1}, \theta) \quad (20)$$

And so we get:

$$\begin{aligned} \frac{\partial \ln P(d|\theta)}{\partial \theta} &= \int P(a|d, \theta) \frac{\partial}{\partial \theta} \sum_{k=1}^N \ln P(a_k|a_{k-1}, \theta) da_1 da_2 \dots da_N \\ &= \sum_{k=1}^N \int P(a|d, \theta) \frac{\partial}{\partial \theta} \ln P(a_k|a_{k-1}, \theta) da_1 da_2 \dots da_N \\ &= \sum_{k=1}^N \int P(a_k, a_{k-1}|d, \theta) \frac{\partial}{\partial \theta} \ln P(a_k|a_{k-1}, \theta) da_k da_{k-1} \end{aligned} \quad (21)$$

$$= \frac{\partial}{\partial \theta} \sum_{k=1}^N \int P(a_k, a_{k-1}|d, \hat{\theta}) \ln P(a_k|a_{k-1}, \theta) da_k da_{k-1} \quad (22)$$

(Note that we define  $P(a_1|a_0, \theta) = P(a_1|\theta)$  and  $P(a_1, a_0|d, \theta) = P(a_1|d, \theta)$ .) Once again – as in (17) and (18), – we have written it out in two ways, (21) and (22), with  $\hat{\theta} = \theta$ , but the hat symbol indicates that when we take the derivative w.r.t.  $\theta$ , that term will not be differentiated.

The term inside the logarithm is just our Markov transition matrix. We already have that term; we'll describe how to find its derivative in section 3.2.5. The weighting terms  $P(a_k, a_{k-1}|d, \theta)$  are fun – the standard forward-in-time Fokker-Planck numerical integration doesn't produce them, so we need to compute them. Fortunately, it turns out that this is readily done.

### 3.2.3 Backward pass to compute the posterior distribution $P(a|d, \theta)$

Here, for simplicity, we'll confine ourselves to the case where the output  $d$  depends only on the last timepoint:  $P(d|a) = P(d|a_N)$ . The model considered in the main text falls into this case. Nevertheless, we point out that it is not difficult to loosen this restriction and still use the approach below.

We need to compute the posterior probability  $P(a|d, \theta)$ . We start with the standard forward-in-time pass, using the Markov transition matrix, that computes  $P(a|\theta)$ . This computation includes the result for  $P(a_N|\theta)$ . From that we can obtain the posterior for the last timepoint:

$$P(a_N|d, \theta) = \frac{P(d|a_N)P(a_N|\theta)}{\int P(d|a_N)P(a_N|\theta)da_N} \quad (23)$$

Now note that the term in (22) that we need to compute is

$$\begin{aligned} P(a_k, a_{k-1}|d, \theta) &= P(a_{k-1}|a_k, d, \theta)P(a_k|d, \theta) \\ &= P(a_{k-1}|a_k, \theta)P(a_k|d, \theta) \\ &= P(a_k|a_{k-1}, \theta) \frac{P(a_{k-1}|\theta)}{P(a_k|\theta)} P(a_k|d, \theta) \end{aligned} \quad (24)$$

The first term in (24) is our Markov transition matrix, which we know; the numerator and denominator in the next term are known from the probability distribution we computed in the forward-pass; and we know the last term for  $k = N$ . Thus we have all we need to compute  $P(a_N, a_{N-1}|d, \theta)$ .

In addition, using the standard equality for a marginal distribution

$$P(a_{k-1}|d, \theta) = \int P(a_k, a_{k-1}|d, \theta)da_k, \quad (25)$$

we see that we can now obtain  $P(a_{N-1}|d, \theta)$ . Which then gives us all we need for the next step backwards in time; and so we keep using (24) and (25), stepping backwards in time, until we have completed a backward-in-time pass and have computed the entire  $P(a|d, \theta)$ . That gives is all the weighting terms we need.

### 3.2.4 Rewriting into matrix notation for discretized spaces

In practice, we are going to work in discretized space. So let's step through rewriting what we've done into discretized space, matrix notation form.

Let's define a vector  $\xi$  whose elements are the positions of the different spatial bins we are using. This is just an index vector that defines the spatial discretization. It will be length  $M$ , where  $M$  is the number of spatial bins. Let's use the indices  $i$  and  $j$  to indicate our spatial bins. Thus we write our forward Markov transition matrix,  $F$  as

$$F_{ij} = P(a_k = \xi_i | a_{k-1} = \xi_j). \quad (26)$$

Let us write the forward probability, marginalized to the  $k^{th}$  timepoint, as

$$f_i^k = P(a_k = \xi_i | \theta). \quad (27)$$

The forward computation is then

$$f_i^k = \sum_j F_{ij} f_j^{k-1} \quad \text{or, in matrix notation,} \quad f^k = F f^{k-1} \quad (28)$$

Let us write the posterior probability (which we compute in the backward pass) as

$$b_i^k = P(a_k = \xi_i | d, \theta) \quad (29)$$

And from (24), let us write a backward propagation matrix

$$B_{ij} = P(a_{k-1} = \xi_i | a_k = \xi_j, d, \theta) = P(a_k = \xi_j | a_{k-1} = \xi_i, \theta) \frac{P(a_{k-1} = \xi_i | \theta)}{P(a_k = \xi_j | \theta)} \quad (30)$$

$$= F_{ji} \frac{f_i^{k-1}}{f_j^k} \quad (31)$$

(Notice that the matrix  $F$  in (31) showed up as its transpose! I.e., as  $F_{ji}$ , not  $F_{ij}$ . It's easy to miss that and forget to take the transpose.) We can now use that backwards propagation matrix for the posterior probability, so that

$$b_i^{k-1} = \sum_j B_{ij} b_j^k \quad \text{or, in matrix notation,} \quad b^{k-1} = B b^k \quad (32)$$

Finally, we write the joint posterior probability distribution over time bin  $k$  and  $k-1$  as matrix  $J^k$ , with elements given by

$$J_{ij}^k = P(a_k = \xi_i, a_{k-1} = \xi_j | d, \theta) \quad (33)$$

$$= P(a_{k-1} = \xi_j | a_k = \xi_i, d, \theta) P(a_k = \xi_i | d, \theta) \quad (34)$$

$$= B_{ji} b_i^k \quad (35)$$

Notice that in this equation for  $J$ , the index  $i$  is for the  $k^{th}$  timepoint, and the index  $j$  is for the  $k-1^{th}$  timepoint. Also,  $B$  shows up as its transpose. Finally, notice that the  $J^k$  and  $F$  matrices are functions of  $\theta$ .

Let us now rewrite (21) and (22) as

$$\frac{\partial \ln P(d | \theta)}{\partial \theta} = \sum_{k=1}^N \sum_{i,j} J_{ij}^k \frac{\partial}{\partial \theta} \ln F_{ij} \quad (36)$$

and

$$\frac{\partial \ln P(d | \theta)}{\partial \theta} = \frac{\partial}{\partial \theta} \sum_{k=1}^N \sum_{i,j} J(\hat{\theta})_{ij}^k \ln F_{ij} \quad (37)$$

where we put  $\hat{\theta}$  in to emphasize that the derivative will apply only to the  $\ln F_{ij}$  term, not to the  $J^k$  matrices.

Now combining (36) and (35), the expression simplifies,

$$\frac{\partial \ln P(d|\theta)}{\partial \theta} = \sum_{k=1}^N \sum_{i,j} \cancel{F_{ij}} \frac{f_j^{k-1}}{f_i^k} b_j^k \frac{1}{\cancel{F_{ij}}} \frac{\partial}{\partial \theta} F_{ij} \quad (38)$$

$$= \sum_{k=1}^N \sum_{i,j} \frac{f_j^{k-1}}{f_i^k} b_j^k \frac{\partial}{\partial \theta} F_{ij} \quad (39)$$

We already know how to compute  $f$  and  $b$ , the prior and posterior distributions. Now all we need is the derivative of  $F_{ij}$ .

### 3.2.5 Differentiating the forward Markov transition matrix for an OU process

In Section 3.1.1.2, we described how to find the forward transition matrix for an OU process defined by equation (11). The derivatives of equation (15) and equation (16) and are:

$$\frac{\partial F_{i=h,j=n}}{\partial s} = \sum_{\xi_h < s < \xi_{h+1}} \frac{-p(s)}{\xi_{h+1} - \xi_h} + \sum_{\xi_{h-1} < s < \xi_h} \frac{p(s)}{\xi_h - \xi_{h-1}} \quad (40)$$

$$\frac{\partial F_{i=h+1,j=n}}{\partial s} = \sum_{\xi_h < s < \xi_{h+1}} \frac{p(s)}{\xi_{h+1} - \xi_h} + \sum_{\xi_{h+1} < s < \xi_{h+2}} \frac{-p(s)}{\xi_{h+2} - \xi_{h+1}} \quad (41)$$

From these expressions, we can derive the derivatives with respect to the three parameters  $\lambda$ ,  $c$ , and  $\sigma^2 dt$ ,

$$\frac{\partial F}{\partial \theta} = \frac{\partial F}{\partial s} \frac{\partial s}{\partial \theta} \quad (42)$$

Specifically,

$$\frac{\partial s}{\partial \lambda} = \frac{\partial \mu}{\partial \lambda} = dt \exp^{\lambda dt} \left( \xi + \frac{c}{\lambda} \right) \quad (43)$$

$$\frac{\partial s}{\partial c} = \frac{\partial \mu}{\partial c} = \frac{1}{\lambda} \left( \exp^{\lambda dt} - 1 \right) \quad (44)$$

$$\frac{\partial s}{\partial \sigma^2 dt} = \frac{s - \mu}{2\sigma^2 dt} \quad (45)$$

Finally, we sum over timepoints  $k$  as in equation (39) to get the final derivative of the log likelihood. The case where parameters vary with time (such as  $c$ , the input to the OU process) requires the construction

of different  $F$  and  $\frac{\partial F}{\partial \theta}$  matrices for each possible combination of parameters, and equation (39) becomes

$$\frac{\partial \ln P(d|\theta)}{\partial \theta} = \sum_{k=1}^N \sum_{i,j} \frac{f_j^{k-1}}{f_i^k} b_j^k \frac{\partial}{\partial \theta} F_{ij}^k \quad (46)$$

*Is computing the gradient worth it?* We have developed the gradient computation for the simple OU process of (11), which has only 3 parameters. The computational cost was  $2X$ , where  $X$  is the cost of a pass ( $2X = \text{forwards pass} + \text{backwards pass}$ ). If we were finding the derivative for 3 parameters using finite differencing, we would need  $4X$ , for four forwards passes. So our approach only gets a factor of 2 in speed-up compared to finite differencing – doesn’t sound very impressive yet. However, the approach holds for OU processes with more parameters (for example, parameters to control mean and variance of the initial position  $a(t=0)$ , a parameter for where the decision boundary is at  $a_N$  is, etc.)– and adding more parameters is essentially cost-free! That’s pretty sweet.

### 3.2.6 Adding sticky decision bounds

Adding sticky decision bounds turns out to be a little tricky, because forward propagation no longer has the simple Gaussian form of (13) – the bound is not at all Gaussian. Taking the sticky bound into account requires a little more bookkeeping. We start by designating  $\xi$  to span  $[-B, B]$  such that its first and last bins now possess the “sticky” property – once probability mass enters one of these bins, it does not leave. Let’s call these bins  $B_L$  and  $B_U$ , for lower and upper bounds, respectively. For simplicity, all spatial bins shall have equal width  $w_i$  except for  $B_L$  and  $B_U$ , for which width is not a meaningful quantity. The positions of  $B_L$  and  $B_U$  are likewise not meaningful; what we need is to have the midpoint between  $B_L$  and the next bin inside the bounds to correspond to the parameter  $B$ . This way of positioning the bins is illustrated in Fig. S15.

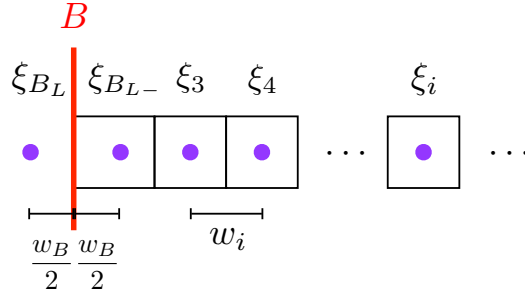


**Fig. S15: Schematic of delineating bins with sticky bounds.** Bins are positioned at constant  $w_i$  from each other, until the next one would exceed the position of the sticky bound  $B$ . An extra  $B_L$  and  $B_U$  is placed outside the lower and upper bounds such that the distance between  $\xi_{B_L}$  and  $\xi_{B_L-}$  is bisected by the desired position of  $B$ . Placed this way, the change in the bin position vector  $\xi$  is all zeros except for its first and last elements, which are  $\partial \xi_{B_L} / \partial B = -2$  and  $\partial \xi_{B_U} / \partial B = +2$ .

Constructing the Markov  $F_{ij}$  matrix with sticky bounds is straight-forward. Inside  $\pm B$ , the Markov process of equation (13) is valid. Probability mass that land outside these bounds are assigned to the bin at the bound. Further, the first and last columns of  $F$  are all zeros except for  $F_{B_L, B_L} = F_{B_U, B_U} = 1$ .



The locations of the sticky bounds  $B$  is a parameter that has been considered constant up until now. Fortunately, the same framework developed in section 3.2.4 is still applicable. Going back again to equation (39), the only additional computation we need is the derivative of the Markov matrix  $F$  with respect to  $B$ , which can be written as

$$\frac{\partial F}{\partial B} = \frac{\partial F}{\partial s} \frac{\partial s}{\partial \xi} \frac{\partial \xi}{\partial B} \quad (47)$$

where we already have  $\partial F/\partial s$  as in section 3.2.5, and  $\partial \xi/\partial B$  is as described in Supplementary Figure 15.

The derivative  $\partial s/\partial \xi$  is

$$\frac{\partial s}{\partial \xi} = \begin{cases} |\xi_{B_{L-}} - s|/(\xi_{B_{L-}} - \xi_{B_L}) & \text{if } B_L < s \text{ and } s < \xi_{B_{L-}} \\ |s - \xi_{B_{U-}}|/(\xi_{B_U} - \xi_{B_{U-}}) & \text{if } \xi_{B_{U-}} < s \text{ and } s < B_U \\ 0 & \text{otherwise} \end{cases} \quad (48)$$

where  $\xi_{B_{L-}}$  is the bin immediately inside  $B_L$  and  $\xi_{B_{U-}}$  is the bin immediately inside  $B_U$ .

### 3.3 The gradient of the log likelihood of the model fit: Implementation

The previous section describes the theoretical framework of the numerical approach; using this approach, we already know how to take the derivative  $\partial P(d_i|t_{i,R}, t_{i,L}, \theta)/\partial \theta$  where  $\theta$  is  $\lambda$ ,  $c$ ,  $\sigma^2 dt$ , and  $B$ .  $\lambda$  and  $B$  appear explicitly as model parameters. This section describes implementing the derivative calculation for the remaining model parameters.

The Poisson click train delivers pulses of evidence at precise moments in time, so that at each timestep, there may be no click inputs or any number of right/left click inputs. It follows that we must construct different  $F$  and  $\frac{\partial F}{\partial \theta}$  matrices at each timestep depending on the number of clicks falling within that  $dt$ , which affects  $c$  (the input magnitude) and  $\sigma^2$  (the variance added).

#### 3.3.1 The derivative with respect to accumulating and sensory noise

The magnitude of variance added per timestep is a sum of accumulating and any applicable sensory noise:

$$\sigma^2 dt = \sigma_a^2 dt + M \sigma_s^2 \quad (49)$$

where  $M = C_R^k + C_L^k$  is the sum of the absolute values of adapted click magnitudes (left and right) falling within this timestep. We know from section 3.2.5 how to obtain  $\frac{\partial F}{\partial \sigma^2 dt}$ , and now we have in addition

$$\frac{\partial \sigma^2 dt}{\partial \sigma_a^2} = dt \quad (50)$$

$$\frac{\partial \sigma^2 dt}{\partial \sigma_s^2} = M = C_R^k + C_L^k \quad (51)$$

Following equation (46), we compute  $\frac{\partial}{\partial \sigma_a^2} F_{ij}^k$  and  $\frac{\partial}{\partial \sigma_s^2} F_{ij}^k$  for each timestep  $k$  and sum over all  $k$  to obtain the derivative of  $\ln P(d|\theta)$ .

### 3.3.2 The derivative with respect to noise in initial conditions

The magnitude of the gaussian distributed initial conditions at time  $t = 0$  is determined by the  $\sigma_i^2$  parameter, but this initial distribution is not part of the dynamics of the model equations. To take the derivative with respect to  $\sigma_i^2$ , we imagine a zeroth timestep before the first timestep and construct a virtual transition matrix  $F_{ij}^{k=0}$  to evolve a delta function  $a = 0$  to a gaussian with variance  $\sigma_i^2$  at the first timestep  $k = 1$ . This zeroth timestep is then treated very much like every other timestep in order to compute the derivative with respect to  $\sigma_i^2$ .

### 3.3.3 The derivative with respect to sensory adaptation parameters

Similarly, the magnitude of the input  $c$  varies at each timestep:

$$c = C_R^k - C_L^k \quad (52)$$

where  $C_R^k$  and  $C_L^k$  are the sums of  $\textcolor{red}{C}$  for right clicks and  $\textcolor{green}{C}$  for left clicks (as defined by equation (6)) for clicks falling within this timestep.

The sensory adaptation parameters also affect the total variance added per timestep:

$$\sigma^2 dt = \sigma_a^2 dt + (C_R^k + C_L^k) \sigma_s^2 \quad (53)$$

$C(t, \phi, \tau_\phi)$  is a function of the click times,  $\phi$  and  $\tau_\phi$ , and it keeps track of the magnitude of a click if one were to play at time  $t$  given all the clicks that played before  $t$ ;  $C_R^k$  is the summed impact of all the right clicks that occurred within time bin  $k$ :

$$C_R^k = \sum_{t=t_R} C(t, \phi, \tau_\phi) \quad (54)$$

where  $t_R$  are the times of the right played with the timestep  $k$ . A corresponding equation exists for  $C_L^k$ .

Section 3.2.5 tells us how to obtain  $\frac{\partial F}{\partial c}$  and  $\frac{\partial F}{\partial \sigma^2 dt}$ , so we need to compute  $\frac{\partial c}{\partial \phi}$ ,  $\frac{\partial \sigma^2 dt}{\partial \phi}$ ,  $\frac{\partial c}{\partial \tau_\phi}$ , and  $\frac{\partial \sigma^2 dt}{\partial \tau_\phi}$ . It is not obvious how this can be done analytically. Fortunately, equation (6) is readily solved analytically in between click times, so we take a pseudo-analytic approach to compute  $\frac{\partial c}{\partial \phi}$  and  $\frac{\partial c}{\partial \tau_\phi}$  using a finite difference method, which is still quit efficient.

To be explicit, let's write out the case for  $\frac{\partial c}{\partial \phi}$ :

$$\begin{aligned} \frac{\partial c}{\partial \phi} &= \frac{\partial C_R^k}{\partial \phi} - \frac{\partial C_L^k}{\partial \phi} \\ &\approx \frac{C_R^k(t, \phi + \Delta\phi, \tau_\phi) - C_R^k(t, \phi, \tau_\phi)}{\Delta\phi} - \frac{C_L^k(t, \phi + \Delta\phi, \tau_\phi) - C_L^k(t, \phi, \tau_\phi)}{\Delta\phi} \end{aligned} \quad (55)$$

and for  $\frac{\partial \sigma^2 dt}{\partial \phi}$ :

$$\begin{aligned} \frac{\partial \sigma^2 dt}{\partial \phi} &= \left( \frac{\partial C_R^k}{\partial \phi} + \frac{\partial C_L^k}{\partial \phi} \right) \sigma_s^2 \\ &\approx \left( \frac{C_R^k(t, \phi + \Delta\phi, \tau_\phi) + C_R^k(t, \phi, \tau_\phi)}{\Delta\phi} - \frac{C_L^k(t, \phi + \Delta\phi, \tau_\phi) - C_L^k(t, \phi, \tau_\phi)}{\Delta\phi} \right) \sigma_s^2 \end{aligned} \quad (56)$$

where  $\Delta\phi$  is some small enough number.

Combining these two effects of the sensory adaptation parameters,

$$\frac{\partial F}{\partial \phi} = \frac{\partial F}{\partial c} \frac{\partial c}{\partial \phi} + \frac{\partial F}{\partial \sigma^2 dt} \frac{\partial \sigma^2 dt}{\partial \phi} \quad (57)$$

These derivatives are used like the others as applied to equation (46).

### 3.3.4 The derivative with respect to bias and lapse rate

Since bias and lapse rate operate outside the scope of equation (5), these derivatives are relatively simple. As illustrated in Fig. S14b, the bias parameter determines the position of the threshold in  $a$  above which a Rightward decision is made. The derivative of  $\ln P(d|\theta)$  with respect to bias can be determined explicitly with a trivial additional computation from the distribution  $p(a, t = T)$ .

The lapse rate parameterizes the probability of making a random response, ignoring equation (5). We implement lapse rate  $L$  by placing  $L/2$  in each of the sticky bound bins at the beginning of the trial, leaving  $1 - L$  in bin  $a = 0$ . Once in the sticky bound bins, this lapse fraction cannot escape, so the same  $L/2$  still contributes to each boundary bin at  $p(a, t = T)$ . We can determine the derivative with respect to lapse rate explicitly by rescaling the  $1 - L$  component of  $p(a, t = T)$ , obtaining what the  $p(a, t = T)$  would be for  $L = L + \Delta L$  with minimal added computation.

## 3.4 Optimization of model parameters

Once we were able to compute the gradient of the log likelihood for each trial (as well as the log likelihood of each trial itself, of course), we then used the sum of these across trials for each rat to obtain the log likelihood of the rat's overall data (equation 4) and its gradient with respect to model parameters. The methods to compute the log likelihood and its gradient were then passed to the `fmincon.m` function from Matlab's optimization toolbox using its interior-point algorithm, which implemented the parameter optimization. The output from `fmincon.m` are the parameter values that maximize the likelihood of the data. Knowledge of the gradient greatly speeds up the parameter search, and was essential to making the search in 9-dimensional space tractable.

Constraints on the parameter search space, unless otherwise specified, were as follows:

- $-5 < \lambda < 5$

- $0 < \sigma_a^2 < 200$
- $0 < \sigma_s^2 < 200$
- $0 < \sigma_i^2 < 40$
- $2 < B < 32$
- $0.1 < \phi < 2.5$
- $0.005 < \tau_\phi < 1$
- $-5 < \text{bias} < 5$
- $0 < \text{lapse rate} < 1$

In the simulations, decision variable variable space had bin sizes of  $dx = 0.25$  q units, and timesteps were  $dt = 0.02$  sec. We found that these bin sizes balanced speed of computation with precision of results.

### 3.5 Confidence interval estimation of the best fit parameters

Having arrived at the best-fit parameters (computation methods described in detail in Sections 3.1 and 3.4), we estimated confidence intervals on these parameters by approximating the likelihood landscape around the best-fit parameters by a multi-dimensional Gaussian distribution [14]. Evaluating the likelihood landscape in a grid around best-fit parameters for a few example subjects (*e.g.*, Fig. 2B-D) confirms that this assumption is locally accurate, except in the sticky bounds  $B$  dimension. Confidence intervals estimated for  $B$  is described separately below.

A one-dimensional Gaussian takes the form  $y \sim \exp(-(x - \mu)^2/\sigma^2)$ , where  $\mu$  is the mean and peak of the distribution, and  $\sigma^2$  is its variance. If the likelihood distribution is approximately Gaussian, then the log likelihood distribution must be approximately quadratic  $\log y \sim -(x - \mu)^2/\sigma^2$ , and the second derivative of this quadratic is the inverse of the variance of the Gaussian. Similarly, for multi-dimensional Gaussians, a quadratic fit to the local log likelihood distribution yields the Hessian, a matrix of second derivatives, whose inverse is the covariance matrix of the locally Gaussian likelihood distribution. We used this strategy to evaluate the quadratic function that fits the multi-dimensional log likelihood landscape around best-fit parameters by least-square regression. The confidence intervals shown in Fig. S5 and Table 2 are 2x std of the multi-dimensional Gaussian marginalized on each parameter.

The likelihood landscape for  $B$  space is not well approximated by a Gaussian. For 17/19 rats and 4/7 human datasets in Fig. S5, increasing the position of the sticky bounds (while holding all other parameters constant at their best-fit values) beyond a certain point did not change the log likelihood of the fits. This makes sense because when for sufficiently large evidence, the likelihood of reversing the side response becomes vanishingly small, even if sticky bounds have not been reached. In this way, all else being equal, even though the probability of hitting the sticky bounds is greater for smaller  $B$ , the total area under the curve (see Fig. S14b, top) on either side of bias threshold is the same as for larger  $B$ . This property that the log likelihood is constant for increasing  $B$  is not a general property of the modeling framework. In other parameter regimes, such as for the burst detector regime illustrated in Fig. 2a, increasing  $B$  greatly

decreases the likelihood of the model fit (Fig. S16). Confidence intervals for  $B$  are determined from a line scan, where the log likelihood is evaluated over different values of  $2 < B < 32$  (all other parameters held at their best fits) and the error bars span the values of  $B$  where the likelihood is larger than 10% of the peak likelihood. If this criterion is met for the largest  $B$  evaluated, then the error bar is considered to extend to infinity.

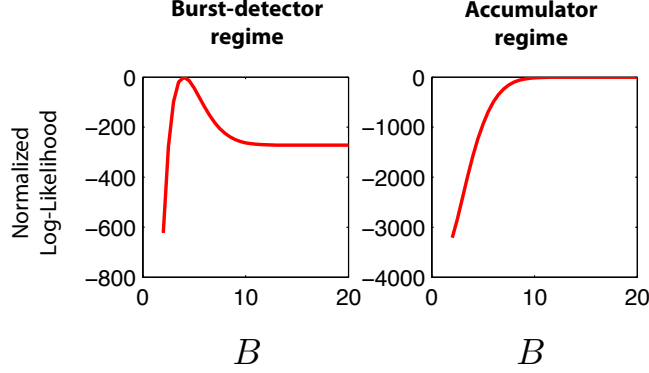


**Fig. S16: Increasing  $B$  decreases log-likelihood of fits in the burst-detector, but not accumulator, parameter regime.**

### 3.5.1 An iterative projection method for computing ill-conditioned Hessians

One numerical challenge to computing multi-dimensional Hessian matrices is when these matrices are ill-conditioned. A matrix is ill-conditioned when its condition number is large, where the condition number is the ratio of the largest to smallest singular value in the singular value decomposition of the matrix. In the context of our log likelihood distributions, the Hessian  $\mathbf{H}$  being ill-conditioned means that the falloff in some dimensions are very sharp, while other dimensions are relatively flat (the range of second derivatives can be  $10^7$  or larger), so it's difficult to estimate this range of second derivatives simultaneously with accuracy. The shape of the log likelihood landscape makes the estimate of its  $\mathbf{H}$  challenging, such that more straight-forward regressions (as well as the Hessian estimated by Matlab's `fmincon.m`) do not accurately represent the log likelihood landscape.

We developed an iterative projection method for computing ill-conditioned Hessians that took advantage of the following observation. The largest eigenvalue of  $\mathbf{H}$ ,  $\lambda_1$ , and its corresponding eigenvector  $\mathbf{v}_1$  are the most accurately estimated by a least-square regression fit of a quadratic function to the log likelihood landscape. Accordingly, we store  $\lambda_1$  and  $\mathbf{v}_1$ , project the Hessian problem onto the subspace minus  $\mathbf{v}_1$ , then re-compute the least-square quadratic regression of the landscape on this new space with one less dimension. This procedure is performed iteratively until 1) the absolute value of the ratio of largest to smallest eigenvalues is small, or 2) there is a one-dimensional subspace remaining.

Let  $\mathbf{V}$  be a square matrix whose  $i$ -th column is the iteratively computed basis eigenvector  $\mathbf{v}_i$ , and let  $\mathbf{\Lambda}$  be a diagonal matrix whose diagonal elements are the corresponding eigenvalues,  $\Lambda_{ii} = \lambda_i$ .  $\mathbf{H}$  can then be reconstructed as  $\mathbf{H} = \mathbf{V}\mathbf{\Lambda}\mathbf{V}^{-1}$ .

## 4 Model-free analyses methods

### 4.1 Psychophysical reverse correlation

The choice-triggered reverse correlation analysis was designed to reveal the epochs of the stimulus that contribute to the decision [15, 5, 16]. Only trials in the top quartile of stimulus durations were included in this analysis, as it is difficult to distinguish different epochs for shorter stimulus durations. First, the local click rates  $\tilde{r}_{i,R}(t)$  and  $\tilde{r}_{i,L}(t)$ , functions of time from start of stimulus, were estimated separately for right and left clicks in each trial  $i$ . This was done by using a causal Gaussian kernel (right half; a click at time  $t_0$  will contribute to traces at times  $t > t_0$ ) to filter delta functions at the times of the clicks  $t_{i,R}$  and  $t_{i,L}$ . The standard deviation of this kernel was  $\sigma = 50$  msec for the auditory tasks and  $\sigma = 100$  msec for the visual task. Because of the filtering artifact at the beginning of the stimulus, the first  $\sigma$  msec of each local click rate trace was ignored. For simplicity, the click rates on either side were collapsed into a single trace:

$$\tilde{r}_i(t) = \tilde{r}_{i,R}(t) - \tilde{r}_{i,L}(t) \quad (58)$$

Trials that had the same generative Poisson rates  $\gamma$  (as defined in section 1.2.1) were grouped and used to compute the median  $\langle \tilde{r}(t) | \gamma \rangle$ , then this trace was subtracted from each trial of that group to arrive at an estimate of the local click rate in excess of what’s expected from trials of the same group:

$$\tilde{R}_i(t) = \tilde{r}_i(t) - \langle \tilde{r}(t) | \gamma \rangle \quad (59)$$

Positive/negative values in  $\tilde{R}$  are parts of the stimulus that had more right/left clicks than expected, respectively.

Traces of  $\tilde{R}_i(t)$  were sorted and separately averaged for trials on which the subject ultimately responded right or left. Epochs of the stimulus that did not inform the response will show right/left reverse correlations that are overlapping and on average zero. In contrast, the reverse correlation traces in epochs of the stimulus important for the response will be significantly separated. As an example, a strongly leaky accumulator with a very short, 50 msec memory ( $\lambda = 1/\tau = -20$ ) will have completely “forgotten” about the beginning of the stimulus by the end, so the reverse correlation traces are only significantly separated at the end (Fig. S17, top). A particularly impulsive accumulator with a similarly short memory ( $\lambda = 1/\tau = +20$ ) will have committed to a decision early in the stimulus, so the end of the stimulus does not correlate with the response (Fig. S17, bottom).

The reverse correlation for each subject is shown in Fig. S10. The red and green shaded plots are the right and left mean traces computed from the rat’s behavioral responses, where the upper/lower extent of the shade plots span the mean  $\pm$  standard error of the mean over trials. The red and green solid lines show results of the identical analysis performed on the best-fit model’s prediction of right and left responses on the same collection of trials. All rats had significantly separated reverse correlation traces for the entire duration of the stimulus; in other words, on average, rats used the the entire stimulus presented to inform their responses. This observation is consistent with long memories as fit by our model.

The reverse correlation analyses for the human subjects were noisier, due to the smaller collection of trials in the dataset, but the same general trend persists.

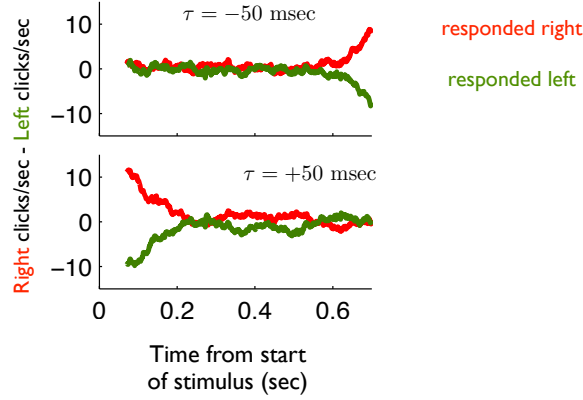


**Fig. S17: Reverse correlation traces for accumulations with very short memories.** The red and green traces are local click rate traces triggered on right and left responses, as described in section 4.1. The top panel shows a leaky accumulator ( $1/\tau = \lambda = -20$ ), which has forgotten the beginning of the stimulus by the end, so the traces are only well separated towards the end. The bottom panel shows an unstable accumulator ( $1/\tau = \lambda = +20$ ), which is impulsive and tends to commit to a decision at the beginning of the stimulus.

## 4.2 Burstiness analysis

Another prediction of the presence of sensory adaptation in the form of click depression is that performance on non-bursty trials should be better than on bursty trials. A number of clicks distributed regularly contributes more net evidence than the same number of clicks distributed in clumps. We looked for this improvement in the rat’s behavior.

First, trials were grouped based on the number of right and left clicks played, so that we are only comparing accuracy on trials of different durations that have the same number of right and left clicks,  $[N_R, N_L]$ . Next, trials that had any inter-click interval (ICI) of less than 10 msec (for rats) on the side of the correct response (the side with a larger total number of clicks, see section 1.2.1) were labeled “bursty,” and all others were labeled “non-bursty.” To exclude the possibility of clicks with very small ICI colliding waveforms confounding this analysis, we took the conservative approach and ignored all trials where there was any ICI less than 2 msec. While there are other possible metrics for burstiness, this simple one was sufficient to detect a decrease in accuracy for bursty trials.

Groups where there was a minimum of 10 trials in each of bursty and non-bursty trials were used for the comparison in accuracy. Figure 2c shows a histogram over groups of the probability correct for non-bursty trials minus the probability correct for bursty trials. The black line marks the median of this distribution, and its statistical significance was tested by a bootstrapping, shuffle test where the “bursty” and “non-bursty” labels within groups were permuted randomly. The grey bar in the right column of Fig. S10 marks the 0.95 confidence intervals of the medians of the random shuffles. The red triangle marks the median of the identical analysis given best-fit model-predicted right/left responses, to be compared with the black line from the rat’s responses. 16/19 rats were significantly more accurate ( $p < 0.05$ ) on non-bursty trials than on bursty trials (Fig. S11).

For analysis of the human datasets, the threshold between a “bursty” and “non-bursty” trials was adjusted to account for the difference in total pulse rates (see sections 1.2.1 and 1.2.3). This threshold was 33 msec for human auditory datasets and 200 msec for human visual datasets. None of the human datasets showed any significant difference in performance between bursty and non-bursty trials.



## 5 Alternative Model: within-stream adaptation

The model described in the main text allows for adaptation effects across both left and right streams—that is, a pulse in one stream can affect the magnitude of the impact of pulses from the other stream. This was chosen so as to allow adaptation parameters to mimic discrimination suppression in the auditory precedence effect<sup>3</sup>. Discrimination suppression refers to the fact that when a click in one ear precedes a click in the opposite ear by  $\approx 5$  to 20 ms, “stimulus parameters of the lag stimulus are less discriminable due to the presence of the lead stimulus” [17].

Nevertheless, a potential alternative model (with the same number of model parameters as the model in the main text), would have the effects of adaptation occurring only within each of the two streams. In such an alternative model, two separate variables,  $C_R$  and  $C_L$  would track the magnitude of the impact of right and left pulses, respectively.

The following equations would then replace equations (1) and (2) of the main text:

$$da = \sigma_a dW + (\delta_{t,t_R}(C_R + \eta_R) - \delta_{t,t_L}(C_L + \eta_L)) dt + \lambda a dt \quad (60)$$

for each of  $R$  and  $L$ :

$$\frac{dC_{R,L}}{dt} = \frac{1 - C_{R,L}}{\tau_\phi} + (\phi - 1)C_{R,L}\delta_{t,t_{R,L}} \quad (61)$$

We fit this alternative model to the data, and found that the model presented in the main text fit the data substantially better (see Fig. S18).

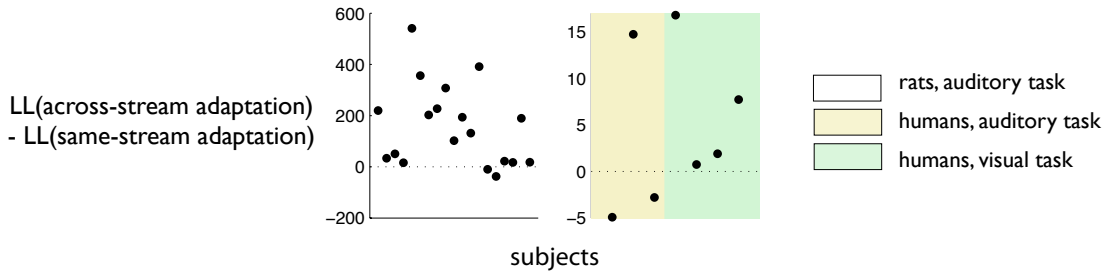


**Fig. S18: Comparison of the model fits using across-stream adaptation versus within-stream adaptation.** Each dot is a subject. The vertical axis represents difference in the log likelihood (LL) for the two models fit to the data of each subject. Positive values favor the model used in the main text.

Nevertheless, our main conclusions, which follow from the values of the best-fit parameters were the same regardless of which of the two models was used. That is, for both models it was true that rats and humans had long accumulator time constants, decision bounds  $B$  large enough to be indistinguishable from infinity,

<sup>3</sup>Other aspects of the precedence effect (“fusion” and “localization dominance”) operate at lags shorter than 5 ms, and only a negligible fraction of the interpulse intervals in our tasks were at those shorter lags. For this reason we focused only on discrimination suppression[17].

and zero accumulator diffusion noise ( $\sigma_a^2 = 0$ ). Again for both models, rats had strong, quickly recovering adaptation, and humans showed weak adaptation in the auditory task while showing weak facilitation in the visual task (see Fig. S19).

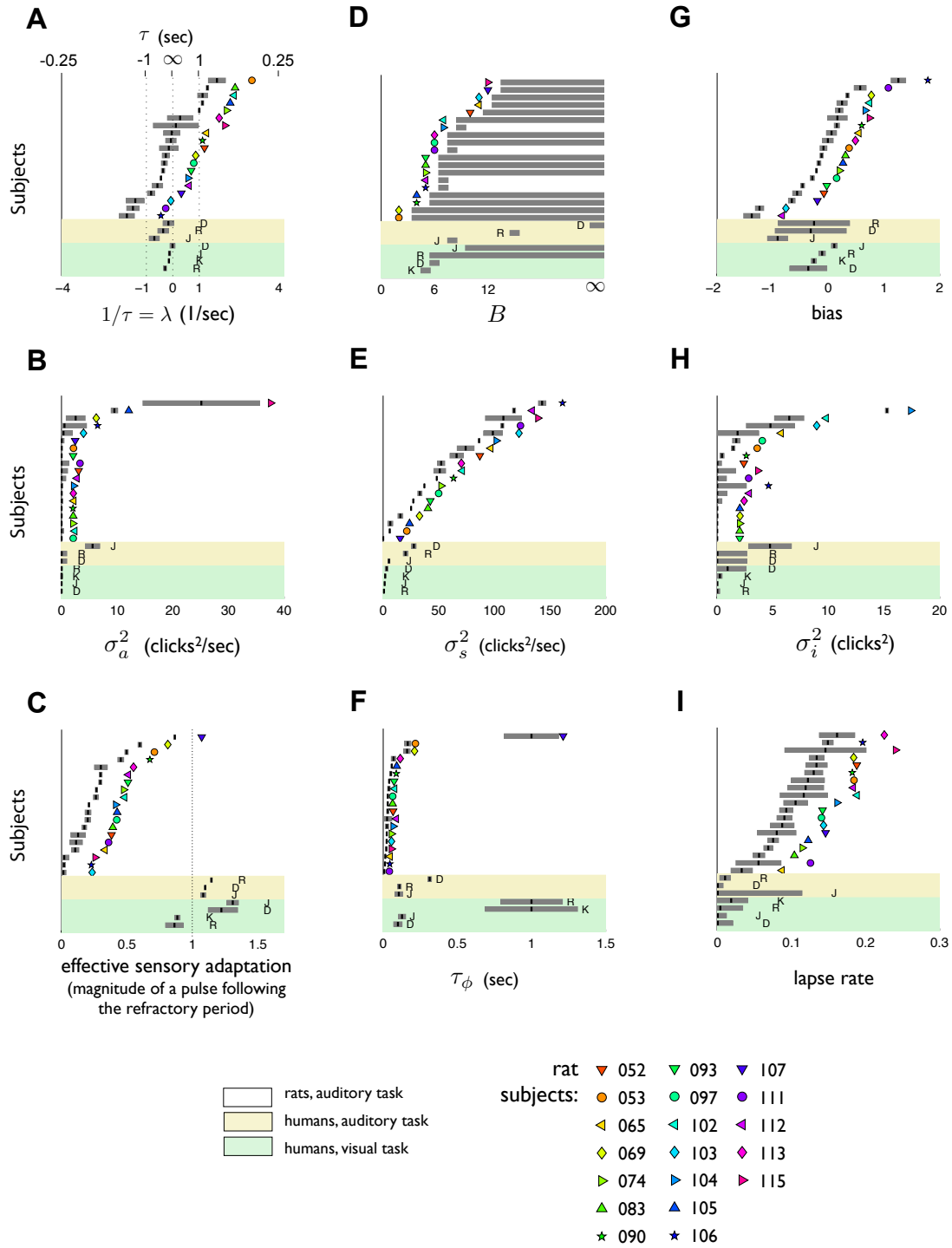


**Fig. S19:** Model fits using a model in which adaptation effects occur independently for the left and right pulse stream (following equation (60) and equation (61)). Format and conventions as in Fig. S5.

## References

- [1] K. V. Nourski and J. F. Brugge, “Representation of temporal sound features in the human auditory cortex,” *Rev Neurosci*, vol. 22, no. 2, pp. 187–203, 2011.
- [2] J. Palmer, A. C. Huk, and M. N. Shadlen, “The effect of stimulus strength on the speed and accuracy of a perceptual decision,” *J Vis*, vol. 5, no. 5, pp. 376–404, 2005.
- [3] R. Ratcliff and G. McKoon, “The diffusion decision model: theory and data for two-choice decision tasks,” *Neural Comput*, vol. 20, pp. 873–922, 4 2008.
- [4] J. D. Roitman and M. N. Shadlen, “Response of neurons in the lateral intraparietal area during a combined visual discrimination reaction time task,” *J Neurosci*, vol. 22, pp. 9475–89, 11 2002.
- [5] R. Kiani, T. D. Hanks, and M. N. Shadlen, “Bounded integration in parietal cortex underlies decisions even when viewing duration is dictated by the environment,” *J Neurosci*, vol. 28, pp. 3017–29, 3 2008.
- [6] J. Ditterich, “Stochastic models of decisions about motion direction: behavior and physiology,” *Neural Netw*, vol. 19, pp. 981–1012, 10 2006.
- [7] W. T. Newsome, K. H. Britten, and J. A. Movshon, “Neuronal correlates of a perceptual decision,” *Nature*, vol. 341, pp. 52–4, 9 1989.
- [8] M. Usher and J. L. McClelland, “The time course of perceptual choice: the leaky, competing accumulator model,” *Psychol Rev*, vol. 108, pp. 550–92, 7 2001.
- [9] R. Kiani and M. N. Shadlen, “Representation of confidence associated with a decision by neurons in the parietal cortex,” *Science*, vol. 324, pp. 759–64, 5 2009.
- [10] R. Ratcliff, “A theory of memory retrieval,” *Psychol Rev*, vol. 85, pp. 59–108, 3 1978.
- [11] L. Paninski, J. W. Pillow, and E. P. Simoncelli, “Maximum likelihood estimation of a stochastic integrate-and-fire neural encoding model,” *Neural Comput*, vol. 16, pp. 2533–61, 12 2004.
- [12] S. Feng, P. Holmes, A. Rorie, and W. T. Newsome, “Can monkeys choose optimally when faced with noisy stimuli and unequal rewards?,” *PLoS Comput Biol*, vol. 5, p. e1000284, 2 2009.
- [13] R. Salakhutdinov, S. Roweis, and Z. Ghahramani, “Optimization with em and expectation-conjugate-gradient,” in *Proceedings of the International Conference on Machine Learning*, vol. 20, pp. 672–679, 2003.
- [14] D. MacKay, *Information Theory, Inference, and Learning Algorithms*. Cambridge University Press, 2003.
- [15] P. Neri, A. J. Parker, and C. Blakemore, “Probing the human stereoscopic system with reverse correlation,” *Nature*, vol. 401, pp. 695–8, 10 1999.
- [16] H. Nienborg and B. G. Cumming, “Decision-related activity in sensory neurons reflects more than a neuron’s causal effect,” *Nature*, vol. 459, pp. 89–92, 5 2009.
- [17] R. Y. Litovsky, H. S. Colburn, W. A. Yost, and S. J. Guzman, “The precedence effect,” *J Acoust Soc Am*, vol. 106, pp. 1633–54, 10 1999.